Probing the electronic and local structure of $Sr_{2-x}La_xCoNbO_6$ using near-edge and extended x-ray absorption fine structures

Ajay Kumar,[1] Rishabh Shukla,[1] Ravi Kumar,[2] R. J. Choudhary,[3] S. N. Jha,[4] and R. S. Dhaka[1,*]

[1]*Department of Physics, Indian Institute of Technology Delhi, Hauz Khas, New Delhi-110016, India*
[2]*Atomic and Molecular Physics Division, Bhabha Atomic Research Centre, Mumbai 400085, India*
[3]*UGC-DAE Consortium for Scientific Research, Indore-452001, Madhya Pradesh, India*
[4]*Beamline Development and Application Section, Physics Group, Bhabha Atomic Research Centre, Mumbai 400085, India*

(Received 24 March 2022; accepted 21 June 2022; published 30 June 2022)

We report the electronic and local structural investigation of double pervoskites $Sr_{2-x}La_xCoNbO_6$ ($x = 0 - 1$) using x-ray absorption near-edge structure (XANES) and extended x-ray absorption fine structures (EXAFS) at the Nb, Co, and Sr K edges. The *ab initio* simulations and detailed analysis of the Nb and Co K-edge XANES spectra demonstrate that the observed pre-edge features arise from the transition of 1s electrons to the p-d hybridized states. We reveal a z-out Jahn-Teller (JT) distortion in the CoO_6 octahedra, which decreases monotonically due to an enhancement in the JT inactive Co^{2+} ions with x. On the other hand, the z-in distortion in NbO_6 octahedra remains unaltered up to $x = 0.4$ and then decreases with further increase in x. This sudden change in the local coordination around Nb atoms is found to be responsible for the evolution of the antiferromagnetic interactions in $x \geqslant 0.6$ samples. Also, we establish a correlation between the degree of octahedral distortion and intensity of the white-line feature in the XANES spectra and possible reasons for this are discussed. More interestingly, we observe the signature of KN_1 double-electron excitation in the Sr K-edge EXAFS spectra for all the samples, which is found to be in good agreement with the $Z + 1$ approximation. Further, the Co $L_{2,3}$ edge shows the reduction in the crystal-field strength and hence an increase in the charge-transfer energy (Δ_{ct}) with the La substitution.

DOI: 10.1103/PhysRevB.105.245155

I. INTRODUCTION

The octahedrally coordinated Co possesses the intriguing magnetic, transport, optical, and electronic properties due to the small energy difference between its various oxidation and spin states [1–3]. The strength of the crystal field (CF) is a crucial measure to govern these properties, as a delicate competition between the Hund's exchange energy and CF splitting decide the electronic distribution in the CF splitted t_{2g} and e_g states [4–6]. In this case, the Co-O bond distance plays the key role in controlling the CF strength. For example, Chen *et al.* have reported a correlation between the Co-O bond length and spin-state transition of Co^{3+} from high-spin (HS) state ($3d^6$; $t_{2g}^4e_g^2$) to the low-spin (LS) state ($3d^6$; $t_{2g}^6e_g^0$) in $SrCo_{0.5}Ru_{0.5}O_{3-\delta}$ using the pressure (hydrostatic) dependent x-ray absorption and emission spectroscopy [7]. It was found that a Co-O bond length >1.93 Å favors the HS state, whereas a smaller value results in the most stable LS state due to the large CF splitting in the latter [7]. Also, an increase in the Co-O-Co bond angle enhances the Co 3d-O 2p orbital hybridization, which stabilizes the intermediate-spin (IS) ($3d^6$; $t_{2g}^5e_g^1$) state of Co in $LaCoO_3$ [8]. On the other hand, the Co^{2+} usually stabilizes in the HS state ($3d^7$; $t_{2g}^5e_g^2$) due to the weaker CF as compared to Co^{3+} in Co-based perovskite oxides [1,2,9]. Thus, a precise understanding of the chemical and local coordination environment around Co and its evolution with the external parameters like temperature, mechanical pressure, and chemical pressure (doping) and hence CF strength is extremely important to engineer the various physical properties of the complex oxides and their vast use in the technological applications [10,11].

In this context, a stable crystal structure of the perovskite oxides [ABO_3; A= rare-earth and alkali earth metals, B = transition metals (TM)] provides a suitable matrix to accommodate the wide range of elements with tunable CF strength and hence degree of TM-O orbital hybridization [12–14]. Further, a 50% substitution of B-site cations results in the alternating ordering of BO_6 and B'(say)O_6 octahedra, where the degree of ordering depends on the ionic and valence mismatch between two B-site cations [15]. This ordering results in the additional B-O-B'-O-B exchange interactions along with the conventional B-O-B channels, resulting in the exotic magnetic and transport properties [16–20]. For example, the antisite disorder-driven several exchange interactions are found to play a crucial role in determining the inverse exchange bias effect observed in Gd_2CoRuO_6 [21]. In the double-perovskite family, the Sr_2CoNbO_6 is one of the most interesting candidates, where high-resolution electron microscopy (HREM) shows the B-site ordered domains of less than 100 Å; however, no such evidence was observed in the x-ray and neutron powder diffraction measurements due to their large coherence length as compared to the size of the ordered domains [9,22]. This is because Sr_2CoNbO_6 is a borderline candidate of the ordered-disordered configurations due to the moderate ionic and valence mismatch between Co^{3+}

*rsdhaka@physics.iitd.ac.in

and Nb^{5+} ions and even a small perturbation can transform it into either regime [15]. This intriguing crystal structure of Sr_2CoNbO_6 is closely related to its observed colossal dielectric properties, complex ac impedance spectroscopy, and cluster-glass-like magnetic ground state [23–25].

Recently, we studied the doping-induced spin-state transition of Co^{3+} from HS to LS/IS state in $Sr_{2-x}La_xCoNbO_6$ ($x = 0 - 1$) samples using the magnetization measurements [9]. Here it is important to note that the substitution of each La^{3+} ion at Sr^{2+} site is expected to transform one Co from 3+ to 2+ state, which systematically reduces the CF strength and stabilizes the Co^{2+} in HS state [1,9,26]. A very small tetragonal ($I4/m$) distortion was observed in the $x = 0$ sample from the perfect cubic ($Pm\bar{3}m$) symmetry, which increases with the La substitution (x) up to $x = 0.4$, and then transformed into the monoclinic ($P2_1/n$) structure for $x \geqslant 0.6$ samples [9]. Further, an increase in the valence mismatch between B-site cations ($\Delta V \approx 2 \rightarrow 3$) with x transform the disordered parent sample to the highly ordered state in the $x = 1$ sample [9]. Importantly, an abrupt enhancement in the B-site ordering and evolution of antiferromagnetic (AFM) interactions were reported for $x \geqslant 0.6$ samples [9,25], which indicate the strong correlation between the local crystal structure and the complex magnetic interactions present in these samples. Also, the specific-heat measurements indicate the persistence of the discrete energy states resulting from the crystal-field splitting, spin-orbit coupling, and octahedral distortion [25]. However, extent of the octahedral distortion, which can play a key role in governing the various spin states of Co^{3+}, and its evolution with the La substitution have not been quantified. Therefore, a systematic study of change in the electronic structure and local coordination around different cations is essential to understand the origin of complex magnetic interactions in these samples. In this direction, x-ray absorption spectroscopy (XAS) is a versatile tool to investigate the ligand field, spin state, valence state, centrosymmetry, metal-ligand overlap, and the local coordination geometry [27].

Therefore, in this paper, we use x-ray absorption spectroscopy to investigate the element-specific electronic and local structure of $Sr_{2-x}La_xCoNbO_6$ ($x = 0 - 1$), and focus on the Nb, Co and Sr K edges in both the x-ray absorption near-edge structure (XANES) and extended x-ray absorption fine structure (EXAFS) regions. The Nb K-edge XANES shows a very weak pre-edge feature in spite of the completely unoccupied $4d$ states, indicating the presence of Nb atoms in the centrosymmetric octahedral environment. However, a strong pre-edge feature is observed in case of Co K-edge XANES spectra, which indicates its off-center displacement in the CoO_6 octahedra. The analysis suggests that pre-edge features in both Nb and Co K-edge spectra result from the transition of $1s$ electrons to the p-d hybridized states. Further, the Co K-edge XANES spectra indicate the deviation of the formal valence state of Co from the expected $(3 - x)$+ state, resulting in the small oxygen nonstoichiometry in the La-rich ($x = 0.8$ and 1) samples. Moreover, we found a strong correlation between the intensity of the white line and degree of octahedral distortion in CoO_6 and NbO_6, where a higher degree of octahedral distortion (compression as well as elongation) results in the reduction of white-line intensity of the respective K-edge absorption spectra. The Co K-edge spectra show the monotonic reduction in the distortion in CoO_6 octahedra with the La substitution (x). However, the Nb K-edge spectra show an abrupt change in the NbO_6 octahedral distortion for $x \geqslant 0.6$ samples, causing a sudden enhancement in the degree of B-site ordering, resulting in the observed AFM interactions at this critical doping. Further, the presence of multielectronic excitation in all the samples in Sr K-edge EXAFS spectra is confirmed using $Z + 1$ approximation as well as La L_3-edge absorption spectra. The Co $L_{2,3}$-edge spectra show the presence of Co^{3+} in the IS/HS state and significant reduction in the crystal-field strength with x.

II. EXPERIMENT

Polycrystalline samples of $Sr_{2-x}La_xCoNbO_6$ ($x = 0 - 1$) were synthesized by usual solid-state route; more details and characterization can be found in Ref. [9]. The x-ray absorption spectroscopic data were recorded at Nb, Co, and Sr K edges in the transmission mode for all the samples using BL-09 (4–25 keV) beam line at Indus-2 synchrotron source (2.5 GeV, 200 mA) at Raja Ramanna Center for Advanced Technology (RRCAT) in Indore, India. The polycrystalline powdered samples were thoroughly mixed in the boron nitride (BN) using a mortar pestle in such a proportion that absorption edge jump ($\Delta\mu$) lies between 0.7 to 1, calculated using the XAFSMASS code [28] and then pressed the total 100-mg powder into the circular disk of ∼15 mm diameter, and sandwiched between the kapton tape for the stability. A Si(111) double-crystal monochromator was used for the precise energy selection of the incident beam with a resolving power of $\Delta E/E \approx 10^{-4}$. More technical details of the beam line can be found in [29]. We calibrate all the recorded spectra using the following energy-dependent relation [27]:

$$E_{\text{calb}} = \frac{gE_{\text{expt}}}{\sqrt{\left(E_{\text{expt}}^2 - g^2\right)}\sin(\Delta\theta) + g\cos(\Delta\theta)}, \tag{1}$$

where E_{calb} and E_{expt} are the calibrated and experimentally recorded energies, respectively, $g \approx 1977.1$ eV for the Si(111) crystal, and $\Delta\theta$ was calculated, by recording the same absorption edge for the reference metal foils, using the equation below:

$$\Delta\theta = \sin^{-1}\left(\frac{g}{E_0}\right) - \sin^{-1}\left(\frac{g}{E_{\text{calc}}}\right), \tag{2}$$

where E_{calc} is the position of the first maxima of the first derivative of the absorption coefficient of the reference metal foil and E_0 is its known reference energy taken at 7709 and 18 986 eV for Co and Nb K edges, respectively, from Ref. [27]. Due to unavailability of the reference metal foil, Sr K-edge spectra were calibrated by aligning the first maxima of the first derivative for the $x = 0$ sample at 16 105 eV (for Sr^{2+} [30]) using the above energy-dependent calibration equations (1) and (2), and then other samples were calibrated with reference to the $x = 0$.

A linear pre-edge and a spline post-edge background were subtracted from the XAS spectra and the resultant spectra were normalized at 800 eV above the edge jump for all the samples. The FEFF9.6.4 code for the *ab initio* calculations, using the full multiple scattering within a sphere around the absorbing atom with the muffin-tin approximation in a

self-consistent loop [31,32], is used to simulate the XANES spectra of Nb, Co, and Sr K edges. The input structural parameters are taken from the refinement of diffraction patterns where the Nb and Co atoms are considered in completely ordered and disordered states at two different B sites for the $x = 0$ and 1 samples, respectively [9,26]. We use Hedin-Lundqvist (HL) exchange-correlation potential to simulate Nb and Co K edges, and Dirac-Hara + HL for Sr K-edge XANES spectra with a fully screened core hole (final-state rule).

The Co $L_{2,3}$-edge and O K-edge XAS spectra were recorded in the total electron yield mode at beam line BL-01of the same synchrotron source. A constant energy shift in each spectra was employed to align the center of L_3 edge of the $x = 0.2$ sample by considering 2.8+ formal valence state of Co as determined by Co K-edge analysis and using Ref. [33], due to the unavailability of the reference sample. The Co $L_{2,3}$ edge is simulated by the CTM4XAS software based on the atomic-multiplet, crystal-field, and charge-transfer approaches [34,35], as the single-electron approach is unable to reproduce the transition metal L-edge XAS spectra. The simulated spectra of HS Co^{2+} and HS Co^{3+} were arbitrarily shifted to align with the $x = 1$ and 0.2 samples, respectively.

III. RESULTS AND DISCUSSION

A. X-ray absorption near-edge structure

The normalized XANES spectra of Nb K edge are presented in Fig. 1(a) for $Sr_{2-x}La_xCoNbO_6$ ($x = 0 - 1$) samples to probe the electronic structure and multiple scattering (MS) mechanism around the Nb atoms. We first discuss the pre-edge region, where no significant intensity is evident around 18 980 eV at the first glance, in spite of the completely unoccupied Nb 4d states ($4d^0$ for Nb^{5+}) in these samples. Note that the low intense pre-edge features in the XANES spectra of TM oxides result from the transition of 1s electrons to the unoccupied pure d states (quadruple transitions; $\Delta l = 2$), and/or transition into the d states hybridized either with their p states or oxygen 2p states [12,36–38]. The probability of the pure quadruple transitions is significantly lower and hence intensity of the pre-edge feature(s) depends mainly on the degree of p-d hybridization [36,37]. The group theory predicts the absence of the p-d mixing and hence the pre-edge feature in case of the ideal octahedral symmetry (O_h), i.e., when absorbing atom lies in the centrosymmetric O_h environment and intensity of the pre-edge features increases with increase in the off-center displacement of the absorbing atoms [36,39,40]. Interestingly, we observe an asymmetricity in the first derivative of the absorption coefficient in the pre-edge region of the Nb K-edge spectra for all the samples as highlighted by the dotted ellipse in Fig. 1(b), which indicates the minimal off-center displacement of the Nb atoms in NbO_6 octahedra. However, the weak pre-edge feature can also result from the thermal-assisted dynamic distortion in the NbO_6 at room temperature, as reported even in centrosymmetric perovskite $EuTiO_3$ [41]. In order to understand the origin of this weak pre-edge feature, the Nb K-edge XANES spectra have been simulated for the $x = 0$ and 1 samples using the FEFF9.6.4 code for a spherical cluster of 45 atoms. Here, it is interesting to note that we have allowed only dipole transitions in the simulations and the weak pre-edge feature is well reproduced in the simulated spectra for both the samples, as compared in Fig. 1(b). In fact, we find that there is no significant enhancement in the pre-edge feature by introducing the quadruple transitions from 1s to the unoccupied d states, as shown in Fig. 1(c). This suggests that the pre-edge feature in all the samples is predominantly due to the dipolar transition from the 1s to the d states of Nb that hybridize with its p states and/or p states of oxygen. To understand further, we plot the d-local density of states (LDOS) for the absorbing Nb atoms (Nb_{abs}) in Fig. 1(b) for the $x = 0$ and 1 samples. Interestingly, we observe a sharp Nb_{abs} d-LDOS at around 18 980 eV corresponding to the weak pre-edge feature, which suggests the key role of the Nb d states in determining the pre-edge feature in these samples. However, a slight discrepancy in intensity behavior between Nb d-LDOS and the simulated spectra is evident in the pre-edge region for the $x = 0$ and 1 samples. The possible reason can be a change in the degree of p-d mixing due to different octahedral distortion in two cases, which is also observed in the EXAFS analysis, discussed in the next subsection. On the other hand, this small change in the pre-edge feature with x is difficult to detect in the experimental spectra.

We now discuss the rising edge (around 18 990 eV) and other features (denoted by 1, 2, 3) observed in the Nb K edge [see Fig. 1(a)]. We note that there is no significant shift in the rising edge position suggesting the invariance in the valence state of Nb with the La substitution. A comparison with the reference Nb_2O_5 sample confirms the pentavalent state of Nb in all the samples [see Figs. 1(a) and 1(b) of [42]]. Further, two prominent features 1 and 2, which are separated by ∼13 eV, can be attributed to the $1s \rightarrow 5p$ transition and the resonance due to multiple scattering of the photoelectrons from the neighboring atoms, respectively [46–48]. It is interesting to note that the intensity of the feature 2 remains almost invariant up to the $x = 0.4$ and then increases monotonically with further increase in the La substitution for the $x \geqslant 0.6$ samples [see inset (a1) of Fig. 1(a)]. This is possibly due to an abrupt change in the local coordination environment around the Nb atoms, which can be speculated as the origin of the evolution of antiferromagnetic interactions in the $x \geqslant 0.6$ samples [9]. We will get back to this point during the discussion of the EXAFS part in the next subsection. Also, a post-edge feature (marked as 3) is observed in all the samples, which shifts towards the higher-energy side [see inset of Fig. 2(a) of [42] for clarity] with a monotonic reduction in its strength [see inset (a2) of Fig. 1(a)] with the La substitution (x). The quantitative changes in the different spectral features with x can be inferred from the Fig. 3(a) and Table I of [42].

In order to understand the origin of the feature 3, in Figs. 1(d) and 1(e), we show the simulated Nb K-edge spectra, which are in good agreement with the experimental spectra in the entire energy range. In fact, the tendency of a doublet around 19 050-19 110 eV turning into the singlet with the La substitution [highlighted by downward arrows in the inset of Fig. 2(a) of [42]] is well reproduced in the simulated spectra. Note that we use a shift of −22.0 eV and an additional broadening of 2.0 eV in the simulation to account for the uncertainty in the Fermi level and core-hole lifetime, respectively. Interestingly, we find that the feature 3 shifts towards

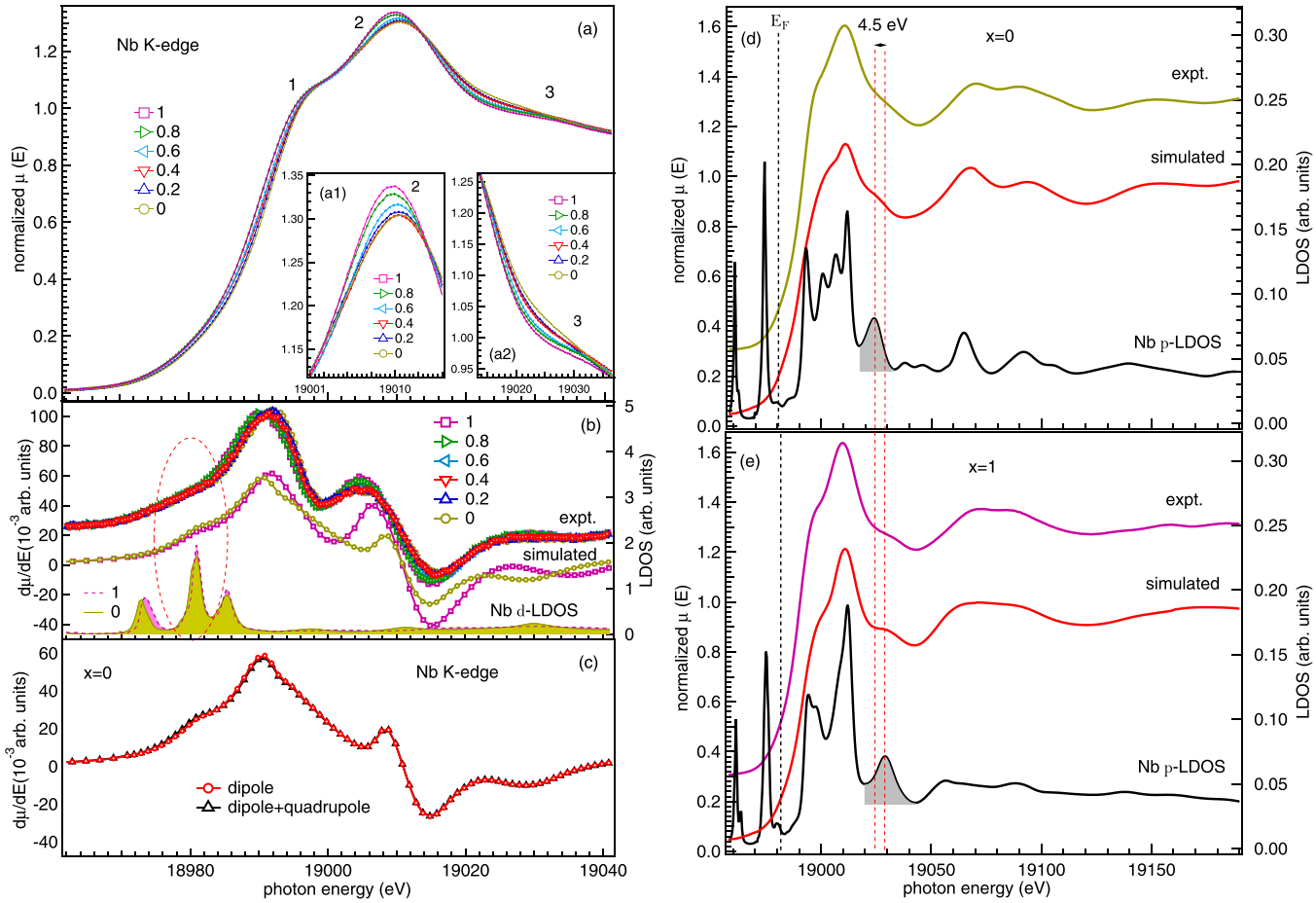

FIG. 1. (a) The normalized Nb K-edge XANES spectra of $Sr_{2-x}La_xCoNbO_6$ ($x = 0 - 1$) samples where 1, 2, 3 represent the main absorption features, and enlarged views of features 2 and 3 are shown in the insets. (b) The first derivative of the experimental absorption spectra of the Nb K edge along the simulated spectrum for the $x = 0$ and 1 samples and their corresponding Nb_{abs} d-LDOS in the XANES region. The red dashed ellipse highlights the presence of pre-edge feature in both experimental and simulated spectra, and sharp Nb_{abs} d-LDOS at this energy. All the experimental spectra have been vertically shifted by fixed 0.025 units for clarity. (c) The comparison of first-order derivative of the simulated absorption coefficient of Nb K edge for dipole, and dipole plus quadrupole transitions for the $x = 0$ sample. (d), (e) The experimental and simulated Nb K-edge absorption spectra along the calculated p-LDOS of absorbing Nb atoms for $x = 0$ and 1 samples. The experimental spectra have been vertically shifted by 0.3 units for clarity. The black dashed line represents the Fermi level and red dashed lines indicate the shift in the Nb_{abs} p-LDOS peak corresponding to the feature 3 (shaded region).

the higher energy with x and to understand this, we plot the Nb_{abs} p-LDOS in Figs. 1(d) and 1(e) for the $x = 0$ and 1 samples, respectively. A clear shift of around 4.5 eV in the unoccupied density of Nb p states corresponding to feature 3 (shaded areas) is observed with x, as highlighted by the red vertically dashed lines, which indicates an increase in the probability of $1s \rightarrow p$ transition at the higher energy in case of the $x = 1$ sample. This perturbation in the unoccupied Nb p-LDOS states with La substitution is originating either from the atomiclike electronic redistribution due to evolution of the new La states or/and from change in the multiple scattering mechanism due to variation in the local coordination environment around the Nb atoms. However, these need to be further explored for complete understanding.

Therefore, we simulate the Nb K-edge XANES spectra for the $x = 0$ sample by selectively removing the neighboring atoms from the spherical cluster. We find a strong dependency of feature 3 on the first-nearest Sr atoms located at 3.430 Å from the absorbing Nb atoms, where the intensity suppressed completely on removal of all the eight first-nearest Sr atoms, as shown in Fig. 2(a) and its inset (a1). More interestingly, the tendency of doublet turning into the singlet in the EXAFS region is also evident on the removal of these Sr atoms, as shown more clearly in the inset (a2) of Fig. 2(a). The corresponding Nb_{abs} p-LDOS are presented in Fig. 2(b), where the inset shows the enlarged view of the highlighted (red dashed rectangle) region corresponding to feature 3. A monotonic reduction in the Nb_{abs} p-LDOS is clearly observed with the removal of first-nearest Sr atoms, which indicates the nonlocal hybridization between the Nb and Sr p orbitals, where an obvious reduction in the Sr p-LDOS is observed around this energy (see Fig. 4 of [42]). A nonlocal orbital hybridization has been widely reported in several correlated electron systems; for example, the presence of Pt and Ir d-LDOS at the different energies causes a shift in the pre-edge peak in the Co K-edge spectra of La_2CoPtO_6 and La_2CoIrO_6 due to Pt/Ir $5d$-Co $4p$ orbital hybridization [49].

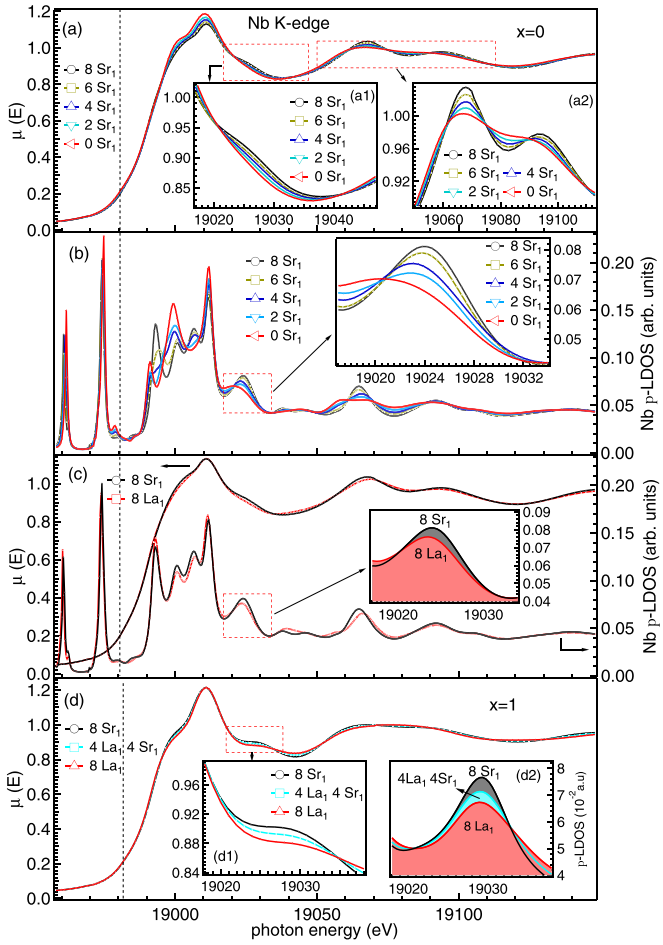

FIG. 2. (a) The simulated Nb K-edge XANES spectra for the $x = 0$ sample by varying the number of first-nearest Sr atoms. Insets (a1) and (a2) represent the enlarged view of the spectra in different energy regimes. (b) The Nb_{abs} p-LDOS corresponding to the XANES spectra presented in (a), and the inset shows the enlarged view of the highlighted region. (c) The comparison of simulated Nb K-edge spectra of the $x = 0$ sample for all first-neighbor A-site atoms as Sr and La (on the left axis) and corresponding Nb_{abs} p-LDOS (on the right axis), and the inset shows the enlarged view of the highlighted region. (d) The Nb K-edge spectra for the $x = 1$ sample with all eight first-neighbor A-site atoms as Sr, four each of La and Sr as well as eight La. The insets (d1) and (d2) represent the enlarged view of the highlighted region and the corresponding Nb_{abs} p-LDOS, respectively.

Further, we observe a small but consistent shift in the Nb p-LDOS towards the lower energy with the removal of the Sr atoms [see inset of Fig. 2(b)], which is opposite to the observation for feature 3 in the experimental data with x. Therefore, in order to disentangle the effect of change in the multiple scattering paths (structure) and evolution of new atomiclike states with x, we present in Fig. 2(c) the simulated Nb K-edge XANES spectra by replacing all the first-nearest Sr atoms by La atoms in the crystal structure of the $x = 0$ sample ($I4/m$ symmetry). A clear reduction in the intensity of feature 3 and corresponding Nb p-LDOS [see inset of Fig. 2(c)] is evident with the La substitution at the first-nearest Sr site. This clearly indicates that the strength of feature 3 depends on the atomiclike states of Sr atoms. However, no shift in the Nb p-LDOS is observed around feature 3 with La substitution. Further, the doublet at the higher energy recovered with the La substitution, indicating the local structure as its origin. In order to further confirm the nature of feature 3, we now use the structural parameters of $x = 1$ sample ($P2_1/n$ symmetry) and simulate the Nb K-edge XANES spectra in three configurations: keeping (i) eight Sr, (ii) four La, and four Sr, and (iii) eight La first-nearest A-site atoms, as shown in Fig. 2(d). We find a reduction in the strength of feature 3 with decrease in the Sr concentration [see inset (d1)], which further indicates its dependence on the atomiclike states of the Sr atoms. On the other hand, no shift in the Nb p-LDOS is observed with change in the nature of first-nearest A-site atoms [see inset (d2)], however, as discussed above, a shift of ~4.5 eV is observed as compared to the $x = 0$ sample. These results suggest that unlike amplitude, the position of feature 3 depends mainly on the arrangement of Nb–La/Sr scattering paths.

In Fig. 3(a) we show the normalized XANES spectra of Co K edge, which show several absorption features (marked A to G) for $Sr_{2-x}La_xCoNbO_6$ ($x = 0 - 1$) samples. The pre-edge feature A around 7710 eV can be attributed to the transitions from $1s$ to $3d$ states of Co, which are mixed with its $4p$ final states and/or $2p$ states of oxygen atoms, where the strength of this pre-edge feature increases with the extent of p-d hybridization [36,37,50]. The presence of the strong pre-edge features in the Co K-edge XANES spectra suggest the higher degree of off-center displacement of Co in the octahedra as compared to the Nb atoms (discussed above). This difference in the local coordination environment around the two B-site cations is also supported by the upcoming EXAFS analysis and useful to understand their complex electronic, magnetic, and transport properties and hence their potential use as the multiferroics [9,23,51,52]. Further, when we increase the La concentration, a significant reduction in the pre-edge feature A is clearly observed along with a monotonic shift towards lower energy [see inset of Fig. 3(a)]. The electron doping in $Sr_{2-x}La_xCoNbO_6$ is expected to transform Co^{3+} into Co^{2+}, which brings the p-d hybridized states of Co closer to the $1s$ states due to increase in the screening effect, resulting in the shift of this quadruple-assisted transition to the lower energy. Additionally, an extra electron doped in the d band of Co ($3d^6$ in Co^{3+} and $3d^7$ in Co^{2+}) results in the reduction of the density of the unoccupied $3d$ states with x, which decreases the transition probability from $1s$ to partially unoccupied $3d$-O($2p$)/Co($4p$) states and consequently the strength of the pre-edge feature A.

Moreover, we observe an enhancement in the intensity of feature B at around 7713 eV with the La substitution [refer Fig. 3(b) and Table I of [42] to see the quantitative changes], as indicated by an arrow in the inset of Fig. 3(a) (also see Fig. 5 of [42] for clarity). These two pre-edge features (A and B) have also been observed in the XANES spectra of $LaCoO_3$ and assigned as the transition from $1s$ state to the crystal-field splitted unoccupied t_{2g} and e_g states of Co in Refs. [5,53]. However, in the present case the Co^{2+} is more likely to exist in the HS state ($3d^7$; $t_{2g}^5 e_g^2$) as compared to Co^{3+} due to weaker crystal field in the former [1,9], which advocates the reduction in the strength of the feature B due to decrease in the density

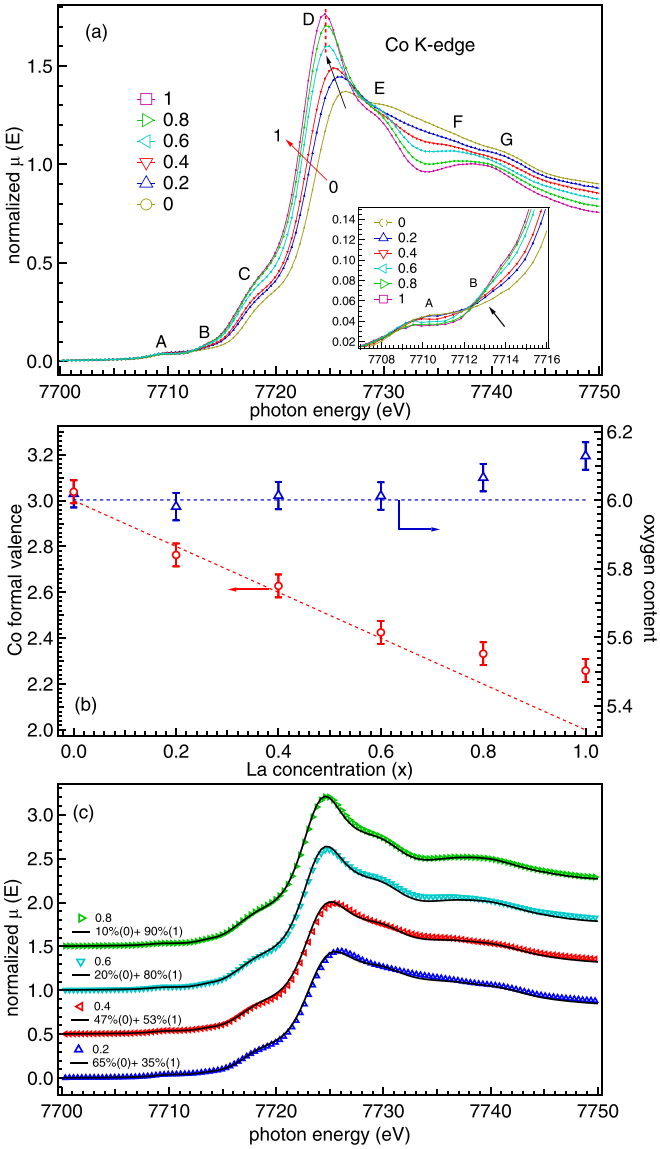

FIG. 3. (a) The normalized Co K-edge XANES spectra of $Sr_{2-x}La_xCoNbO_6$ ($x = 0 - 1$) samples. The letters A–G represent the absorption features resulting from various electronic transitions (see text for the detail). The red arrow indicates the shift in the rising edge towards the lower energy with the La substitution. The solid black arrow and dashed red line represent the shift and invariance in the white line for x $\leqslant$ 0.4 and $x \geqslant 0.6$ samples, respectively. Inset shows the enlarged view of the A and B (arrow) pre-edge features for clarity. (b) The average oxidation state of Co (open circles) on left axis and oxygen concentration (open triangles) on the right axis, as a function of x. Dashed red and blue lines represent the ideal behavior for the full transformation of Co from 3+ to 2+ valence state (considering the linear relationship between shift in edge position and oxidation state) and six oxygen atoms per formula unit, respectively. (c) The Co K-edge XANES spectra for the intermediate compositions, i.e., $x = 0.2$–0.8 samples, where the solid black lines represent the Co valence state weighted linear combination of the $x = 0$ ($Co^{3.0+}$) and $x = 1$ ($Co^{2.25+}$) spectra. Each spectrum is vertically shifted cumulatively by 0.5 units for clarity.

of unoccupied e_g states with the La substitution, contrary to the observation as just discussed above. This discards the transition from 1s to pure e_g states of Co as the origin of this second pre-edge feature B. In this line, based on the charge-transfer multiplet calculations, Vankó *et al.* assigned this second feature B as the dipolar transition from 1s to Co(4p)-O(2p)-Co′(3d) hybridized states in $LaCoO_3$, where Co′ represents the next-nearest Co ions [54]. This hypothesis was further supported by the angular independence of the intensity of this second feature (B) in the x-ray absorption study on the epitaxial thin films of $LaCoO_3$ [55]. Here, the enhancement in the strength of feature B with the La substitution indicates that the latter hypothesis is clearly favored in the present case. Also, the higher transition probability from 1s state to the Co(4p)-O(2p)-Nb(4d) hybridized states as compared to Co(4p)-O(2p)-Co′(3d) states can be the possible reason for the enhancement in the strength of this feature B, as alternating ordering of CoO_6 and NbO_6 octahedra increases with the La substitution [9].

The feature C around 7717 eV is attributed to the charge transfer from oxygen to Co ions in the final state due to strong Co 3d-O 2p orbital hybridization, indicating the small charge-transfer energy (Δ_{ct}) in these compounds, i.e., $1s^1\underline{c}3d^6L^2 \rightarrow 1s^1\underline{c}3d^7\underline{L}^1$ process, where $\underline{c}$ and $\underline{L}$ represent the core and ligand holes, respectively. For example, Chainani *et al.* found the ground state of $LaCoO_3$, an octahedrally coordinated Co^{3+} perovskite, to be 38.5% in $1s^1\underline{c}3d^6L^2$, 45.4% in $1s^1\underline{c}3d^7\underline{L}^1$, and 14.5% even in $1s^1\underline{c}3d^8\underline{L}^2$ state from their x-ray photoemission spectroscopic measurements [56]. A small but consistent reduction in the feature C is observed with the La substitution [see Fig. 3(b) and Table I of [42]], which indicates a decrease in the tendency of charge transfer from ligand to metal. A decrease in the valence state of Co and increase in Co-O bond distances (as evident from the EXAFS analysis, discussed later) with the La substitution can result in the enhancement of the Δ_{ct} and hence reduction in the intensity of feature C. This reduction in the orbital overlapping can also be the possible reason for decrease in the electronic conductivity of these samples with x [9]. A similar correlation between the electronic conductivity and orbital hybridization was observed from the XAS measurements of the $Sr_{2-x}Nd_xCr_{1+x/2}Re_{1-x/2}O_6$ samples [57].

It is important to note that a monotonic shift in the rising edge (region between features C and D) is observed towards the lower energy, as indicated by red arrow in Fig. 3(a), which indicates the changes in Co valence state from 3+ towards 2+ with the La substitution. A comparison with the Co K-edge XANES spectra of reference $LaCoO_3$ sample [58] indicates the valence state of Co close to 3+ in the $x = 0$ sample, as shown in Fig. 6 of [42]. Note that an overall shift of 2.5 eV is reported for the complete transformation of Co from 3+ to 2+ state [59,60], which is used to quantify the formal valence state of Co as a function of La substitution in all the samples, due to the unavailability of the reference sample for pure Co^{2+}, as shown on the left axis of Fig. 3(b). Here, we consider a linear relationship between the shift in the absorption edge position and change in the valence state of Co [61], where

the absorption edge position (E_0) is taken at $\mu d = 1$ for all the samples. The red dashed line in Fig. 3(b) represents the linear behavior for the full transformation of Co from 3+ to 2+ valence state. The extracted values of the formal valence state of Co follow this linear relationship up to the $x = 0.6$ sample, whereas a small enhancement (oxidation of Co) is observed for the $x = 0.8$ and 1 samples. This deviation in the valence state of Co from the 2+ can be the possible origin for the weak FM interactions observed in the $x = 1$ sample [9], as Co^{2+} is AFM in the octahedral environment [2]. The extracted Co valence state of 2.25 ± 0.05 in case of the $x = 1$ sample suggests that the reduction of Co below this is energetically less favorable than the presence of oxygen nonstoichiometry in these La-rich samples. Therefore, we estimate the oxygen concentration from the Co valence states, as the valence states of La^{3+}, Sr^{2+}, and Nb^{5+} are invariant, and present on the right axis of Fig. 3(b). The blue dashed line represents the oxygen stoichiometric condition with six oxygen atoms per formula unit, where a small deviation (δ) is observed in case of the $x = 0.8$ and 1 samples with $\delta = 0.07$ and 0.13, respectively. The presence of excess oxygen and hence oxidation of the transition metal cations was also reported in several other perovskite oxides [59,62–64]. However, deducing the oxygen content from the Co valence state in the present case is a naive approximation due to the significant Co $3d$-O $2p$ orbital hybridization, as evident from the strong pre-edge features in the Co K-edge XANES spectra as well as the *ab initio* simulations, discussed later.

For the intermediate ($x = 0.2$–0.8) compositions, the Co is present in the mixed valence states where either all the Co atoms can exist in the nonintegral intermediate valence states or can fluctuate between the valence states of two end members ($x = 0$ and 1) [65]. In order to disentangle this, in Fig. 3(c) we compare the XANES spectra of the intermediate compositions with the linear combination of $x = 0$ ($Co^{3.0+}$) and $x = 1$ ($Co^{2.25+}$) spectra, keeping the average oxidation state of Co equal to that presented in Fig. 3(b). A good agreement between the experimental and weighted sum spectra of the two end members is observed for all the intermediate compositions, even the post-edge features and white-line intensity reproduces well. This behavior indicates that the valence state of the intermediate compositions is fluctuating between those of the two end member samples, i.e., between $Co^{3.0+}$ (for $x = 0$) and $Co^{2.25+}$ (for $x = 1$). These results reveal that the mixed valence states of Co in these samples belong to the class II of Robin and Day classification, i.e., the electronic cloud is delocalized, but still the two sites of Co (with different formal charges) are distinguishable [65].

Moreover, the most prominent feature D around 1725 eV is attributed to the most probable $1s \rightarrow 4p$ dipole transition. A monotonic shift in this feature to the lower energy is observed from $x = 0$ to 0.4, as indicated by the black arrow in Fig. 3(a), whereas this feature remains almost invariant with the further La substitution for $x \geqslant 0.6$ samples (vertical red dashed line). Note that the position of the white line depends not solely on the valence state but also on the local coordination environment around the absorbing atom [51]. A structural transition from the tetragonal to the monoclinic phase was reported in these samples for $x \geqslant 0.6$ from our previous x-ray and neutron powder diffraction measurements [9,66]. Thus, a cumulative effect of both valence shift and structural transformation results in the minimal shift in the feature D for the $x \geqslant 0.6$ samples. Further, the strength of this feature increases with a monotonic reduction in the peak broadening, which indicates a decrease in the disorders in these samples with x. This is because the disorders result in the statistically varying energy states, which broaden the spectra, whereas f-sum rule states that the overall integrated intensity of the absorption spectra remains constant, irrespective of the final state [67], causing a reduction in the peak height [60]. A similar variation in the nature of the white line has been reported in the Ti K-edge absorption spectra of various complex oxides with the varying degree of the disorders in [37], where a comparison between the crystalline, radiation-damaged, and glassy $CaTiSiO_5$ clearly demonstrates the increase in the broadening and decrease in the main-edge peak height with reduction in the crystallinity [37]. A variation in the white line of the Co K-edge XANES spectra of $Sr_{2-x}La_xCoNbO_6$ is more clearly illustrated in Fig. 7 of [42]. In the present case, reduction in the octahedral distortion (in CoO_6) as well as B-site disorders with x can be the possible origin for this monotonic enhancement in the intensity of the white line of Co K-edge XANES spectra. On the other hand, the Nb K-edge XANES spectra show no significant variation in the intensity of the white line up to $x = 0.4$ [see inset (a1) of Fig. 1(a)]. Note that the influence of the B-site disorders on the main-edge feature is expected to remain the same for both Co and Nb K-edge spectra. This clearly demonstrates that the intensity of white line is solely governed by the degree of the octahedral distortion, which is also evident from the EXAFS analysis, discussed later.

We find the systematic decrease in strength of post-edge features (E, F, and G) of Co K-edge XANES spectra with x. For example, the evolution of a valley between E and F features is clearly observed in Fig. 3(a). Using the spin-polarized DOS calculations, Pandey *et al.* assigned the similar post-edge features in the Co K-edge XANES spectra of $LaCoO_3$ as the transition of Co $1s$ electrons to Co $4p$ states hybridized with the La $6p$ and/or O $2p$ states [68]. In the present case, our analysis of the FEFF simulations suggests that a decrease in the O $2p$ states in the post-edge region causes a reduction in theses features (particularly feature F) with the La substitution (see Fig. 8 of [42]). Here it is important to reemphasize the fact that transformation of Co from 3+ to 2+ state with the La substitution decreases the extent of orbital overlapping between Co and oxygen atoms due to weaker CF in the latter. This reduces the delocalized nature of the Co p states and hence the strength of post-edge features in the Co K-edge XANES spectra with x.

Now we move to the discussion of the Sr K-edge XANES spectra [see Fig. 4(a)] to probe the chemical environment and local structure around the A-site atoms and its evolution with La substitution. There is no signature of pre-edge peak even in the first derivative of the absorption coefficient (not shown) for all the samples. The inset (a1) of Fig. 4(a) shows the first derivative of the absorption coefficient in the rising edge region, where no significant shift (as indicated by the vertical dashed line) indicates the invariance in the valence state of Sr with x. Further, the most intense feature, marked as I, is attributed to the dipole-allowed $1s \rightarrow 5p$ transitions, which vary nonmonotonically with x. Interestingly, the intensity of

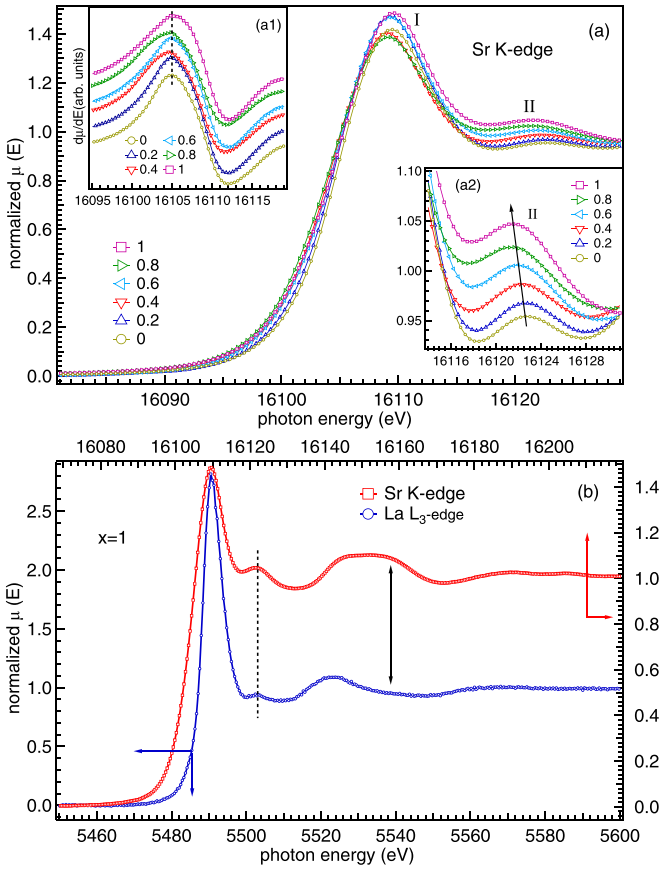

FIG. 4. (a) The normalized Sr K-edge XANES spectra of $Sr_{2-x}La_xCoNbO_6$ ($x = 0 - 1$) samples. The inset (a1) shows the first derivative of the absorption coefficient, where the vertical dashed line represents the invariance in the rising edge position. These curves are vertically shifted for better presentation. The inset (a2) presents the enlarged view of feature II, where the arrow shows the shift in the peak position with x. (b) The normalized Sr K-edge (on top and right axis) and La L_3-edge (on bottom and left axis) spectra for the $x = 1$ sample in 150-eV range in the vicinity of the white line. The dashed line represents the presence of the absorption feature II at the same position with respect to the white line in both the spectra.

post-edge feature II increases significantly with x, as shown more clearly in the inset (a2) of Fig. 4(a). Also, a shift in feature II towards lower energy is clearly observed with x, as shown by the arrow in inset (a2) [see Fig. 3(c) and Table I of [42] for the quantitative changes]. A similar post-edge feature in the La L_3 and Sr K-edge XANES spectra has been observed in $La_{2-x}Sr_xCuO_4$ samples, which is attributed to the removal of apical oxygen around the absorbing atoms with Sr substitution [69]. However, this hypothesis was later contradicted by the theoretical calculations by Wu *et al.* [70]. In order to understand the origin of this feature, La L_3-edge XANES spectrum has been recorded for the $x = 1$ sample and compared with Sr K edge in Fig. 4(b). The presence of similar absorption features above the white line in case of La L_3-edge XANES spectra [see vertical dashed line in Fig. 4(b)] discard the atomiclike states of Sr as the origin of this feature. This suggests that the multiple scattering from the neighboring atoms gives rise to the feature II in these samples. The *ab initio* simulations of the Sr K-edge XANES spectra indicate that the feature II originates from the multiple scattering from 12 nearest-neighbor oxygen atoms, where any change in the Sr-O scattering paths with the La substitution alter the oxygen p-LDOS at this energy, and hence intensity and position of the feature II [see Figs. 9(a) and 9(b) of [42] and discussion therein]. Also, a comparison of the La L_3-edge spectra of the $x = 1$ sample with the reference La_2O_3 sample indicates the presence of La in the trivalent state (see Fig. 10 of [42]). However, the low La concentration unable us to record the good quality La L_3-edge XAS spectra for the other samples, which can be complementary to the Sr K-edge spectra.

B. Extended x-ray absorption fine structures

Having discussed the electronic structure, we now focus on the EXAFS part of XAS spectra to understand the local coordination environment around different elements in these samples. In Fig. 5(a), we show the amplitude of the Fourier transformed $k^3\chi(k)$ of high-resolution EXAFS spectra of Nb K edge for all the samples and the normalized raw data are presented in Fig. 2(a) of [42]. The background-subtracted EXAFS spectra are fairly smooth up to $k \approx 14$ Å^{-1} (see Fig. 11 of [42] for the $x = 0$ sample), allowing us to probe even the small spectral features from the higher coordination shells with reasonable accuracy. In Fig. 5(a), the first intense maxima around 1.5 Å (phase uncorrected) is attributed to the Nb-O scattering paths in the NbO_6 octahedra. It is interesting to note that the intensity of this maxima remains almost constant for $x \leqslant 0.4$ samples and then it increases monotonically with further increase in the La substitution, analogous to the variation in intensity of the white line observed in the Nb K-edge XANES spectra [see inset (a1) of Fig. 1(a)]. Here, it is important to note that in the tetragonal ($I4/m$) symmetry, the four equatorial (O_e; in ab plane) and two axial (O_a; along c axis) oxygen positions lead to the two sets of different Nb-O bond distances [71]. Invariance in the peak intensity corresponding to Nb-O scattering path indicates almost no change in the degree of NbO_6 octahedral distortion for the $x \leqslant 0.4$ samples. This is also evident from the local distortion parameter (Δ_d) around the Nb atom (denoted by Δ_{Nb}) (see Table I), quantified using the equation [72]

$$\Delta_d = \frac{1}{n}\sum_{i=1}^{n}\left(\frac{d_n - \langle d\rangle}{\langle d\rangle}\right)^2, \tag{3}$$

where n is the number of atoms coordinated to that site, d_n is the bond length between that site and nth coordinated atom, and $\langle d\rangle$ is the average bond length of all the coordinations to that site. In the monoclinic ($P2_1/n$) symmetry for $x \geqslant 0.6$ samples, four Nb-O_e bonds further split in two sets of different bond distances. However, in order to avoid overparametrization, we assume the identical Nb-O_e bond distances in the EXAFS fitting, as shown in Figs. 5(h)–5(m) for the $x = 0 - 1$ samples, respectively. Here, an increase in the intensity of the Nb-O scattering path for $x \geqslant 0.6$ samples [see Fig. 5(a)] indicates the statistically narrow distribution of the Nb-O path lengths, i.e., decrease in the octahedral distortion (in NbO_6) for these samples (see Δ_{Nb} values in Table I). This is found to be interesting as the NbO_6 octahedra accommodate the

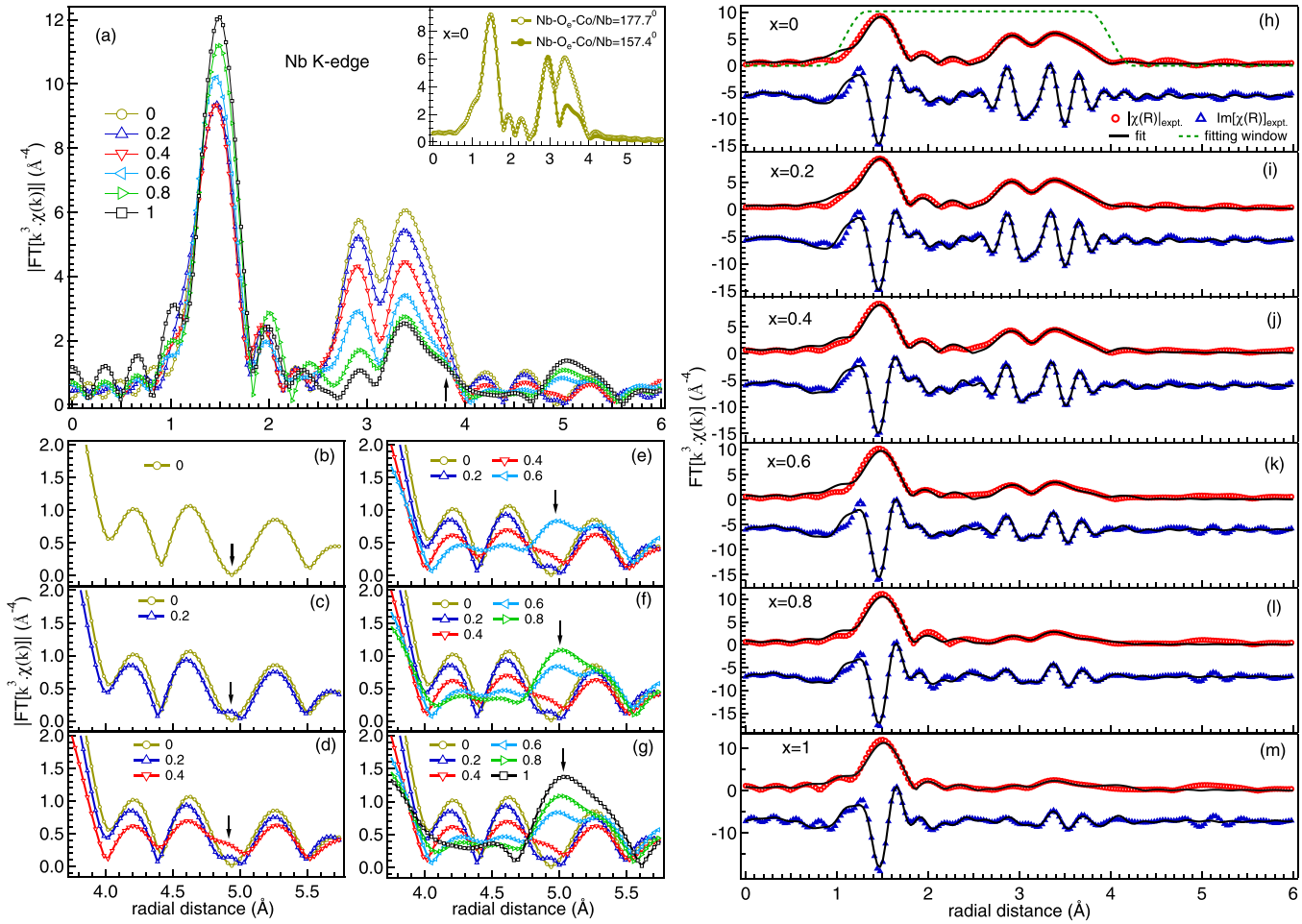

FIG. 5. (a) The magnitude of the Fourier-transformed $k^3\chi(k)$ spectra for $Sr_{2-x}La_xCoNbO_6$ ($x = 0 - 1$) in 0–6 Å spectral range, derived from the EXAFS region of the Nb K edge. The inset shows the comparison of simulated spectra of the $x = 0$ sample for two different Nb-O_e-Co/Nb angles (Nb-O_a-Co/Nb = 180°). (b)–(g) The enlarged view of (a) between 3.75 to 5.75 Å with cumulative increment in x to clearly show the evolution of an additional scattering path resulting from the Co/Nb atoms, located diagonally to the absorber, as indicated by the arrows (refer text for more details). (h)–(m) The fitting of the $|\chi(R)|$ and corresponding Im$[\chi(R)]$ spectra in the window shown by the dotted green line, each Im$[\chi(R)]$ spectrum is shifted downward for clarity in presentation.

chemical pressure exerted by the substitution of smaller La^{3+} ions at the Sr^{2+} site [73] up to the $x = 0.4$ sample. However, with further increase in x, the NbO_6 octahedra rotate around the x and y axes with the same magnitude, leading to the monoclinic distortion having $b^-b^-c^+$ tilt [9,26,66], which results in the abrupt decrease in the distortion of NbO_6 octahedra for the $x \geqslant 0.6$ samples. This is also manifested by the sudden enhancement in the B-site ordering (refer Table I and discussion below) and hence antiferromagnetic interactions in $x \geqslant 0.6$ samples through Co-O-Nb-O-Co 180° superexchange path [9]. Further, this abrupt change in the local coordination around Nb atoms for $x \geqslant 0.6$ samples can be the possible reason for the different nature of thermal expansion of the unit cell for the $x = 0.4$ and 0.6 samples, as observed using neutron powder diffraction (NPD) in Ref. [66].

The second and third maxima at around 2.9 and 3.4 Å are attributed to the Nb–Sr/La and Nb–Co/Nb scattering paths, respectively. Interestingly, the intensity of both the scattering paths suppresses with x, where Nb–Sr/La path decreases more rapidly as compared to Nb–Co/Nb path [see Fig. 5(a)]. The La substitution at Sr site results in the evolution of new Nb-La scattering paths at a different radial distance as compared to Nb-Sr paths. Also, a structural distortion [from tetragonal ($I4/m$) to monoclinic ($P2_1/n$) phase] resulting from the La substitution causes splitting in the eight equal Nb-Sr scattering paths, and consequently a reduction in the strength of the corresponding feature in $|\mathrm{FT}[k^3\chi(k)]|$ plot. However, the EXAFS is unable to resolve these spatially close ($\Delta r < 0.02$) Nb–Sr/La scattering paths and such a close statistical distribution in the path lengths is incorporated in the enhancement of Debye-Waller (DW) factor (σ^2) corresponding to that path. Here, we assume the same DW factor for Nb-Sr and Nb-La scattering paths to fit the Nb K-edge EXAFS spectra. A small enhancement in the Nb–Sr/La scattering path length is also observed with x [see Fig. 5(a)]. Here, a competition between decrease in the ionic radii of A-site cations ($r_{La^{3+}} = 1.36$ Å and $r_{Sr^{2+}} = 1.44$ Å; 12 coordinated [73]) and increase in the Coulombic repulsion between Nb^{5+}-Sr^{2+}/La^{3+} ions with x govern this scattering path length and the dominance of the latter effect results in the observed enhancement in this scattering path length with x. Further, the Nb–Co/Nb scattering paths are

mediated by the oxygen atoms and hence forward scattering paths Nb-O–Nb/Co–Nb are more favorable as compared to the single scattering (SS) Nb–Co/Nb paths. The x-ray diffraction patterns clearly evidence that structural distortion due to La substitution causes significant deviation in the Nb-O–Co/Nb bond angle (from ≈179° in $x = 0$ to ≈158° in the $x = 1$ sample [9]), which transform Nb-O–Nb/Co–Nb forward scattering path into an obtuse triangle with the lower scattering amplitude. This results in the reduction in both the MS paths through Nb atoms, causing the observed monotonic reduction in the corresponding peaks in $|\mathrm{FT}[k^3\chi(k)]|$ plot [see Fig. 5(a)]. In order to confirm this, we simulate the $|\mathrm{FT}[k^3\chi(k)]|$ spectra for the $x = 0$ sample by varying the Nb-O_e–Co/Nb angle from 177.7° to 157.4°, keeping all the other parameters constant, as shown in the inset of Fig. 5(a). A significant reduction in the spectral weight around 3.5 Å clearly indicates that the oxygen-mediated MS path is the origin of this feature. A similar change in the pseudoradial distribution function is reported in $Sr_{2-x}Ca_xYIrO_6$ samples with change in the Y-O-Ir angle [74]. Also, it is important to note that in a completely *B*-site disordered structure, each Nb atom is statistically coordinated with 3 Co and 3 Nb first-nearest *B*-site neighbors, whereas in case of fully ordered structure, each Nb atom is coordinated with six Co atoms [21,75]. Here, the coordination number of the first-nearest Nb atoms (N_{Nb}) and the resulting order parameter $S = (3 - N_{\mathrm{Nb}})/3$ from the best fit of the EXAFS spectra are listed in Table I, where $S = 0$ and 1 represent the completely disordered and ordered structures, respectively. A clear enhancement in the *B*-site ordering with the La substitution is evident from Table I. We use the same zero-energy shift parameter (ΔE_0) and many-body amplitude reduction factor ($S_0^2 = 0.8$) for all the scattering paths to fit the Nb *K*-edge EXAFS spectra of $Sr_{2-x}La_xCoNbO_6$ samples. Moreover, we consider a single-scattering path Nb-O2 [where O2 indicate the second-nearest oxygen atoms; see Fig. 12(a) of [42]] at around 3.8 Å causing an asymmetry in the peak at the higher radial distance, as indicated by the arrow in Fig. 5(a). This asymmetry appears to become more prominent as the intensity of the main peak at 3.4 Å reduces with increase in the x.

More importantly, a close inspection in the range of ∼4–5.6 Å clearly indicates the evolution of different spectral features, as shown in Figs. 5(b)–5(g) cumulatively with x. Here, the feature around 4.6 Å is resulting from the Nb–La/Sr–O2-Nb double-scattering path. As discussed above, the splitting in Nb–Sr/La scattering paths with the La substitution provides the statistically wide range of path lengths for their corresponding MS paths, causing the observed consistent reduction in the intensity of this peak. Further, a feature around 5.3 Å is resulting from the Nb-O3 single-scattering path, as shown in Fig. 12(b) of [42]. Another interesting observation is the evolution of an additional feature around 5 Å with the La substitution, as indicated by arrows in Figs. 5(b)–5(g). This feature is resulting from the single scattering from second-nearest *B*-site atoms (Nb–Co2/Nb2), i.e., along ⟨110⟩ directions of pseudocubic unit cell, as shown in Figs. 12(c) and 12(d) of [42]. The completely random occupancy of Co and Nb atoms at two Wyckoff positions in case of the $x = 0$ sample and its minimal deviation from the cubic symmetry results in the absence of this feature in Fig. 5(b), as Nb–Co2/Nb2 SS path is mediated by the central Sr atoms in the perfectly symmetric environment. Further, a reduction in the crystal symmetry with the La substitution, as also speculated from the deviation in the tolerance factor (τ) from unity [9], results in the evolution of this feature with x, as shown in Figs. 5(b)–5(f). This is consistent with the evolution of new Raman active modes in these samples with the La substitution [9]. Further, an abrupt increase in the strength of this feature for the $x \geqslant 0.6$ samples [see Figs. 5(b)–5(g)] is consistent with the structural transition from tetragonal ($I4/m$) to the monoclinic ($P2_1/n$) structure accompanied by the sharp enhancement in the *B*-site ordering (see Table I) at this critical doping ($x = 0.6$), which is correlated with the degree of octahedral distortion in the NbO_6 unit, as discussed above. Although the consistent variation in these features with the La substitution up to the radial distance of around 6 Å (phase corrected) clearly indicates the high data quality, we fitted the EXAFS spectra up to 4 Å to improve the reliability in the extracted parameters. It is important to note that despite the overall enhancement in the structural distortion, the distortion in the NbO_6 octahedra decreases with the La substitution.

Now we discuss the effect of La substitution on the local coordinate environment around the Co atoms. In Fig. 6(a), we show the amplitude of the Fourier transformed $k^3\chi(k)$ of Co *K*-edge EXAFS spectra for all the samples. The normalized raw data are plotted in Fig. 2(b) of [42] along with the other details. The most prominent feature around 1.5 Å results from the Co-O scattering paths. The intensity of this feature increases monotonically with the La substitution, unlike Nb-O scattering path in the Nb *K*-edge EXAFS spectra, which remains constant up to $x = 0.4$ [see Fig. 5(a)]. This suggests a different evolution of local coordination environment around the Co and Nb atoms with the La substitution. Here a higher degree of octahedral distortion results in the low intense wider peak in the $|\chi(R)|$ distribution function as compared to the Nb *K*-edge spectra. Importantly, the increase in the intensity of this feature at 1.5 Å is consistent with the variation in the strength of white line of Co *K*-edge XANES spectra [see Fig. 3(a)], analogous to the correlation observed in the Nb *K* edge. The fitted Co *K*-edge EXAFS spectra are presented in Figs. 6(d)–6(i) and the best fit parameters are provided in Table I. We observe the z-out distortion in the CoO_6 octahedra, which decreases with x, in spite of the reduction in the crystal symmetry (see Δ_{Co} values in Table I). This indicates the presence of electronic instability assisted Jahn-Teller (JT) distortion in these samples, as the intermediate spin (IS) state of Co^{3+} ($t_{2g}^5 e_g^1$) is JT active [58,76]. This z-out distortion in the CoO_6 octahedra is expected to cause the observed z-in distortion in the neighboring NbO_6 octahedra (see Table I), which is consistent with the temperature-dependent NPD measurements performed on the $x = 0.4$ and 0.6 samples [66]. However, the distortion parameter (Δ) around the *B*-site atoms extracted from the NPD measurements for the $x = 0.4$ sample is significantly higher at all the temperatures (50 ± 5) [66], as compared to the values presented in Table I. Note that the $x = 0.4$ sample shows the high degree of the antisite disorders (swapping between the Co and Nb atoms at the two Wyckoff positions) and NPD gives the average distortion at the *B* sites, whereas in the present case the EXAFS analysis provides the actual distortion around the particular absorbing atoms.

TABLE I. The EXAFS fitting parameters for $Sr_{2-x}La_xCoNbO_6$ samples extracted from the Nb, Co, and Sr K-edge spectra.

x	0	0.2	0.4	0.6	0.8	1
			Nb K edge			
R_{Nb-O_e} (Å)	2.024(2)	2.025(3)	2.038(1)	2.028(4)	2.020(1)	2.023(2)
$\sigma^2_{Nb-O_e}$ ($\times 10^{-3}$ Å^2)	4.1(3)	4.5 (1)	5.7(2)	4.7(1)	4.1(1)	4.1(1)
R_{Nb-O_a} (Å)	1.914(2)	1.915(3)	1.924(4)	1.925(1)	1.928(1)	1.939(2)
$\sigma^2_{Nb-O_a}$ ($\times 10^{-3}$ Å^2)	0.2(2)	0.3(2)	0.2(2)	0.2(4)	0.3(2)	0.2(3)
$\Delta_{Nb} \times 10^{-4}$	6.8(2)	6.8(3)	7.2(4)	5.9(4)	4.8(1)	3.9(2)
R_{Nb-Sr} (Å)	3.431(2)	3.436(2)	3.435(4)	3.451(1)	3.436(1)	3.498(4)
$\sigma^2_{Nb-Sr/La}$ ($\times 10^{-3}$ Å^2)	7.8(1)	7.5(3)	8.5(4)	9.6(1)	7.9(1)	10.3(2)
R_{Nb-La} (Å)	–	3.439(2)	3.480(6)	3.460(1)	3.426(3)	3.481(4)
$R_{Nb-O-Nb-Nb}$ (Å)	3.771(2)	3.782(3)	3.781(1)	3.806(4)	3.722(3)	3.822(6)
$\sigma^2_{Nb-O-Nb-Nb}$ ($\times 10^{-3}$ Å^2)	5.4(1)	4.4(3)	6.7(4)	4.6(2)	6.3(5)	4.5(5)
N^{Nb}	3.0(1)	2.9(0)	2.7(1)	1.2(1)	0.7(0)	0.3(1)
S	0.00(3)	0.03(1)	0.10(3)	0.60(3)	0.77(1)	0.90(3)
R factor	0.013	0.013	0.017	0.027	0.019	0.019
			Co K edge			
R_{Co-O_e} (Å)	1.925(3)	1.932(4)	1.935(1)	1.968(2)	2.020(6)	2.023(1)
$\sigma^2_{Co-O_e}$ ($\times 10^{-3}$ Å^2)	8.9(2)	8.3(4)	7.6(2)	6.3(1)	4.5(4)	4.4(1)
R_{Co-O_a} (Å)	2.059(2)	2.059(3)	2.058(2)	2.085(1)	2.134(5)	2.126(1)
$\sigma^2_{Co-O_a}$ ($\times 10^{-3}$ Å^2)	5.7(2)	4.6(4)	2.6(2)	1.8(1)	1.5(2)	2.1(1)
$\Delta_{Co} \times 10^{-4}$	10.3(3)	9.2(4)	8.6(2)	7.5(2)	6.8(6)	5.6 (1)
R_{Co-Sr} (Å)	3.655(2)	3.676(4)	3.623(1)	3.551(1)	3.541(3)	3.517(1)
$\sigma^2_{Co-Sr/La}$ ($\times 10^{-3}$ Å^2)	11.6(2)	10.1(5)	18.2(3)	18.0(6)	18.6(3)	17.5(1)
R_{Co-La} (Å)		3.640(4)	3.693(1)	3.651(1)	3.633(5)	3.650(1)
$R_{Co-O-Co-Co}$ (Å)	3.899(2)	3.889(3)	3.835(1)	3.781(4)	3.776(7)	3.937(2)
$\sigma^2_{Co-O-Co-Co}$ ($\times 10^{-3}$ Å^2)	5.4(1)	7.4(3)	8.3(1)	4.9(2)	4.2(5)	5.0(5)
R factor	0.007	0.024	0.017	0.013	0.029	0.015
			Sr K edge			
R_{Sr-O_1} (Å)	2.560(2)	2.543(2)	2.534(1)	2.535(3)	2.522(4)	2.519(1)
R_{Sr-O_2} (Å)	2.668(2)	2.670(1)	2.671(2)	2.618(2)	2.639(3)	2.563(2)
R_{Sr-O_3} (Å)	2.857(3)	2.848(1)	2.870(2)	2.844(2)	2.837(4)	2.803(1)
$\sigma^2_{Sr-O_1/O_2/O_3}$ ($\times 10^{-3}$ Å^2)	9.2(3)	6.9(2)	8.7(3)	11.5(1)	10.3(4)	13.6(3)
$R_{Sr-Co/Nb}$ (Å)	3.315(2)	3.327(2)	3.347(1)	3.415(2)	3.451(5)	3.453(2)
$\sigma^2_{Sr-Sr/La}$ ($\times 10^{-3}$ Å^2)	5.8 (1)	8.8(2)	12.1(2)	12.7(3)	13.0(4)	11.1(1)
$R_{Sr-Sr/La}$ (Å)	3.473(2)	3.482(1)	3.483(2)	3.486(1)	3.463(5)	4.500(2)
$\sigma^2_{Sr-Sr/La}$ ($\times 10^{-3}$ Å^2)	8.8(1)	8.8 (2)	9.1(2)	11.4(3)	11.8(4)	16.2(1)
R factor	0.012	0.014	0.008	0.011	0.019	0.010

Moreover, a decrease in the DW factor of the Co-O scattering paths is observed with x, suggesting the reduction in both static as well as dynamic distortion around the Co atoms. An enhancement in the concentration of Co^{2+} ions with the La substitution results in the reduction of this z-out JT distortion in the CoO_6 octahedra, as Co^{2+} is more likely to exist in the JT inactive HS state as compared to Co^{3+} [1,9]. However, this simplified hypothesis based on the pure ionic picture may partially break down due to the covalent character of Co-O bond, resulting from the higher crystal field in these samples. For example, an increase in the occupancy of $3d$ states (more than six electrons for Co^{3+}) and the partial occupancy of e_g states has been reported even for the LS configuration of $LaCoO_3$ [77,78]. Note that the increase in ionic radius of Co (0.545 Å for LS and 0.610 Å for HS Co^{3+}, and 0.650 Å for LS and 0.745 Å for HS Co^{2+}; 6 coordinated [73]) and decrease in the Coulombic attraction between oxygen and Co atoms results in the shift of Co-O scattering part to the higher radial distance with the La substitution, as shown by the red arrow in Fig. 6(a). Further, a feature around 3.2 Å is attributed to the Co–La/Sr scattering path. Here, we find that the strength of this feature as well as the scattering path length reduces with x, as shown by the black arrow in Fig. 6(a). However, note that the strength decreases, but the scattering path length increases with x in case of Nb–La/Sr, as observed and discussed above. Here, a cumulative effect of increase in the ionic radii of Co ($r_{Co^{2+}} > r_{Co^{3+}}$), decrease in that of A-site cations ($r_{La^{3+}} < r_{Sr^{2+}}$), and reduction in the Coulombic repulsion between Co and A-site cations govern the evolution of Co–La/Sr scattering path length with the La substitution (x). The dominance of the latter two effects results in the observed reduction in this scattering path length with x, as shown in Fig. 6(a). Another peak at the higher radial distance of around 3.7 Å is resulting from the nearest-neighbor Co–Nb/Co scattering paths. The fitting of the Co K-edge EXAFS spectra is performed in 1–4 Å range, with the same procedure as described above for the Nb K-edge EXAFS analysis. Here, we use the same degree of the B-site ordering (i.e., fraction of the first-neighbor Co atoms)

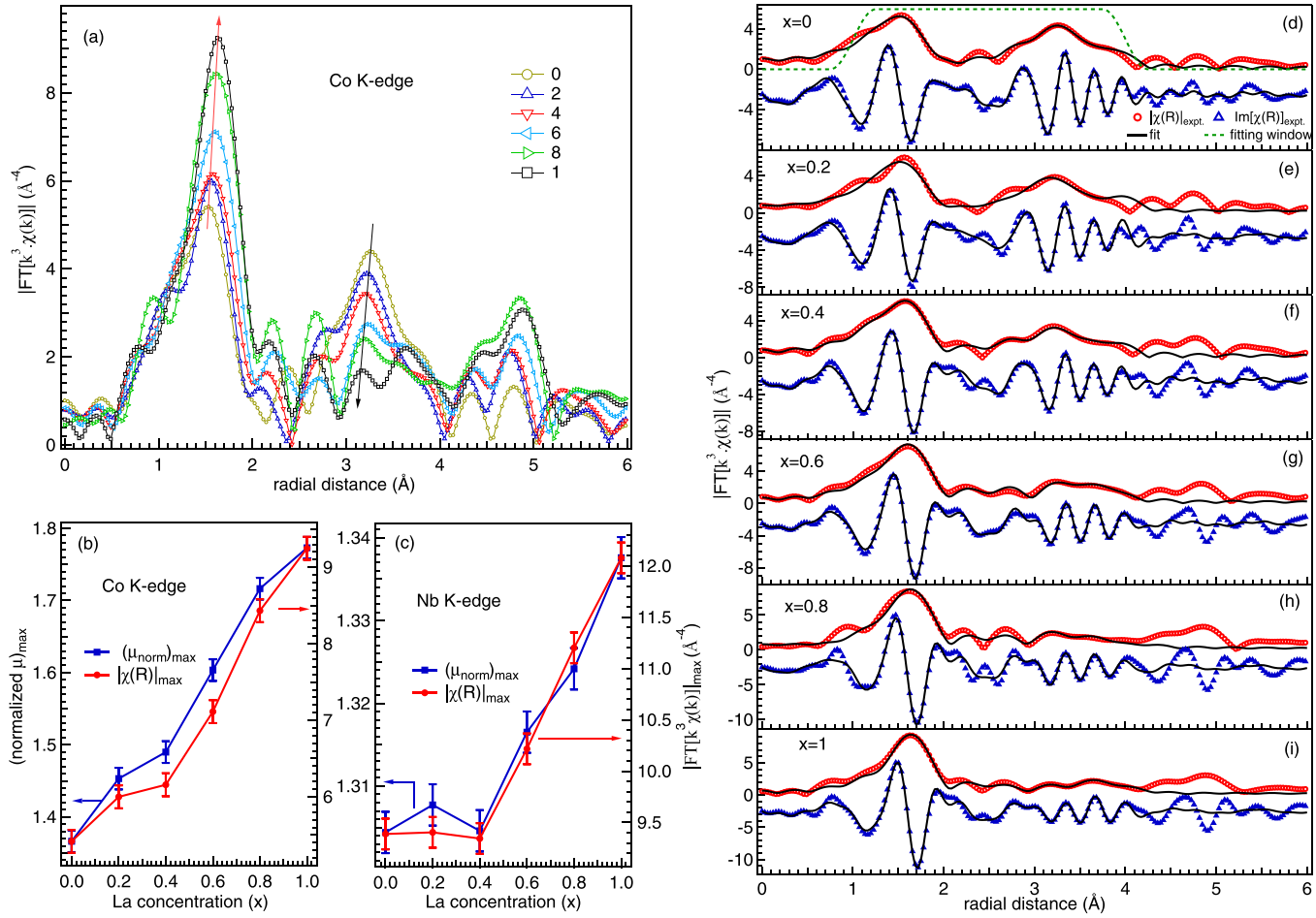

FIG. 6. (a) The magnitude of the Fourier-transformed $k^3\chi(k)$ spectra for $Sr_{2-x}La_xCoNbO_6$ ($x = 0 - 1$) in 0–6 Å spectral range, derived from the EXAFS spectra of Co K edge. (b) The evolution of the intensity of the white line (left axis) and amplitude of the first coordination shell (right axis) with the La substitution for the Co K-edge and (c) Nb K-edge EXAFS spectra. (d)–(i) The fitting of the $|\chi(R)|$ and corresponding $\mathrm{Im}[\chi(R)]$ spectra in the window shown by the dotted green line, where the $\mathrm{Im}[\chi(R)]$ spectrum in each panel is shifted downward for clarity in the presentation.

as extracted from the Nb K-edge EXAFS spectra in order to improve the reliability in the other fitting parameters.

To further interpret the behavior of main feature at ≈1.5 Å in the EXAFS spectra, i.e., the change in the degree of distortion in the CoO_6 and NbO_6 octahedra with the La substitution, we compare the magnitude of Co-O and Nb-O scattering paths with the respective white-line intensity in the Co and Nb K-edge XANES spectra in Figs. 6(b) and 6(c), respectively. A strong correlation between the intensity of white line and degree of the octahedral distortion can be clearly observed, irrespective of the direction of octahedral distortion in two cases. In order to understand this we simulate the Nb K-edge XANES spectra for the $x = 0$ sample by varying the extent of octahedral distortion in NbO_6 unit, as shown in Fig. 7(a). Here, only Nb-O_a and Nb-O_e scattering path distances were varied in order to systematically enhance the Δ_{Nb}, keeping all the other structural parameters constant. We find a systematic reduction in the intensity of the white line with increase in the octahedral distortion, as shown in the inset (a1) and plotted quantitatively in the inset (a2) of Fig. 7(a). The corresponding intensity of Nb p-LDOS also shows the monotonic reduction with increase in the value of Δ_{Nb} as indicated by the arrow in Fig. 7(b). The increase in the degree of the octahedral distortion is expected to enhance the orbital hybridization between Nb and oxygen states, and can result into the spatially wide distribution of the Nb p states. The FEFF code simultaneously calculates the charge on the different valence orbitals and the resulting charge transfer from the initial neutral atoms [79], which can be useful to understand the electronic structure of the underlined compounds and its evolution with the different perturbations, as presented in Table II for the selected atoms. Here, the Δe represent the charge transfer within the Norman radius at the time of the self-consistent calculations, which is the difference between the total l-projected charge count and number of valence electrons in the free atoms (considered one additional electron in the valence state of absorbing Nb, accounting for the core hole) [80,81]. Note that the Δe values are much smaller than the underlined oxidation state of Nb and O atoms in the sample, but these can be used to qualitatively understand the variation in the electronic structure with Δ_{Nb}. Also, the octahedral oxygen environment around the absorbing Nb atoms give rise to the sp_3d_2 type hybridization, causing a decrease in s and increase in the p and d orbital electron counts as compared to the free Nb and

TABLE II. The charge transfer (Δe) and charge counts in the s, p, and d states of Nb_{abs} and O atoms extracted from the simulation of the Nb K-edge XANES spectra of the $x = 0$ sample by varying Nb-O bond distances.

Nb-O_a(Å) →		1.990	1.980	1.970	1.960	1.950	1.940	1.930	1.920
Nb-O_e(Å) →		1.990	2.000	2.010	2.020	2.030	2.040	2.050	2.060
Nb_{abs}	s	0.392	0.392	0.391	0.390	0.389	0.387	0.386	0.385
Nb_{abs}	p	6.603	6.602	6.601	6.600	6.598	6.598	6.597	6.5967
Nb_{abs}	d	4.143	4.151	4.164	4.175	4.184	4.194	4.204	4.213
Nb_{abs}	Δe	0.861	0.855	0.844	0.836	0.828	0.821	0.813	0.806
O	s	1.835	1.836	1.835	1.835	1.835	1.834	1.834	1.834
O	p	4.498	4.496	4.492	4.488	4.485	4.481	4.477	4.473
O	d	0.074	0.075	0.076	0.077	0.078	0.079	0.080	0.081
O	Δe	-0.408	-0.407	-0.403	-0.400	-0.397	-0.394	-0.391	-0.387

O atoms [$s = 1(2)$, $p = 6(4)$, $d = 4(0)$ for the Nb(O)] [80]. Importantly, the value of Δe decreases with increase in the octahedral distortion for both Nb as well as oxygen atoms, which indicates the enhancement in the degree of orbital overlapping between these two atoms, resulting in the deviation from the free-ion-like character of Nb atom. Further, an increase in the difference between Nb-O_e and Nb-O_a bond distances enhances the spatial distribution of Nb p states (hybridized with the O $2p$ states) and hence decreases the strength of the white-line feature. This hypothesis suggests that the pure $1s \rightarrow np$ transition as an origin of the white line in the K-edge XANES spectra is an over- simplified assumption and the effect of the molecular orbitals on the XANES features of the transition elements should also be stressed. For example, the change in the XANES spectra of the transition metal oxides with varying degree of electronegativity has been well explained by Modrov *et al.* on the basis of the molecular orbital theory [80]. Also, the presence of several absorption features in the oxygen K-edge spectra (see Fig. 13 of [42]) indicates the strong metal-ligand hybridization in these samples.

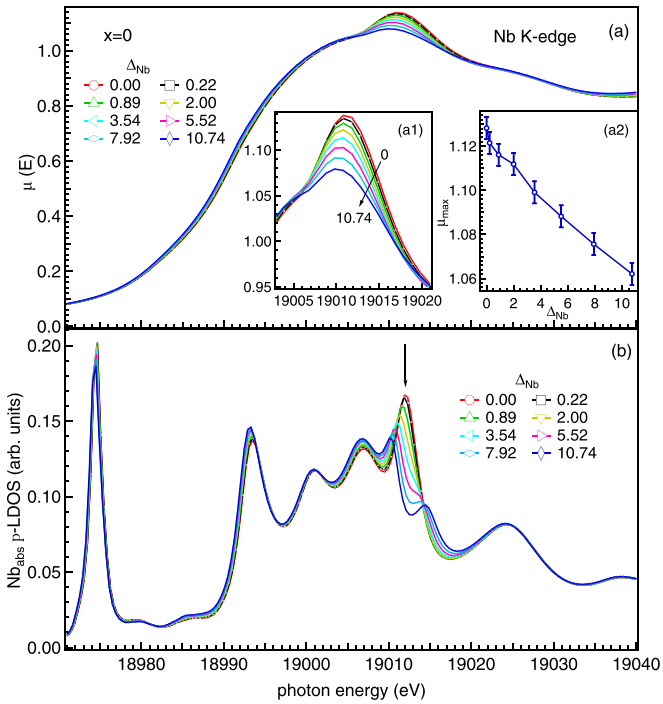

FIG. 7. (a) The Nb K-edge XANES spectra simulated for the $x = 0$ sample by varying the degree of distortion in NbO_6 octahedra. The insets (a1) and (a2) represent the enlarged view of the white line and variation of the white-line intensity with the distortion parameter Δ_{Nb} defined in Eq. (3), respectively. The error bars in the white-line intensity in inset (a2) are accounting for the finite step size of the simulated spectra. (b) The corresponding Nb_{abs} p-LDOS simulated at different values of Δ_{Nb} for the $x = 0$ sample.

In Fig. 8(a) we present the magnitude of the Fourier transformed $k^3\chi(k)$ of Sr K-edge spectra to investigate the local coordination environment around the A-site cations. Interestingly, an intense peak is observed at a very small radial distance of around 0.8 Å, which is smaller even than the ionic radii of Sr^{2+} cation in the 12-fold coordination environment [73] and, hence, no scattering path is expected at this position. These features at the low radial distances are usually not associated with the local structural arrangement of the atoms, but arise mainly due to the multielectronic transitions within the atoms, which can appear well above the white line in the absorption spectra and mix with the EXAFS oscillations [82–85]. The inaccurate treatment of these spectral features can lead to the significant error in structural parameters extracted from the EXAFS analysis. In case of Sr K-edge absorption spectra, an intra-atomic excitation from $1s$ to $4s$ (KN_1) states results in the sharp absorption feature well above the white line [82]. The position of this feature can be estimated by the $Z + 1$ approximation, where binding energy of the Sr ($Z = 38$) electrons in the different levels can be approximated by that of yttrium ($Z = 39$) after the ejection of one photoelectron from the K shell. This approximation predicts the KN_1 double-electron excitation at 43.8 eV above the Sr K-edge threshold energy [82]. Interestingly, a sufficiently intense feature is clearly observed at 44.4(4) eV above the threshold energy of Sr K edge in all the samples, as shown in Fig. 8(b) for the $x = 0$ sample [see inset in Fig. 2(c) of [42]]. The absence of this feature above the white line of the La L_3-edge spectra, as indicated by the black arrow in Fig. 4(b) for the $x = 1$ sample, clearly indicates the atomiclike states of the Sr atom as its origin rather than the local atomic arrangement around the Sr atoms. Therefore, a careful treatment of the Sr K-edge EXAFS spectra is necessary for the accurate structural probe. In order to further confirm the origin of this low radial distant peak in Fig. 8(a), we subtract the KN_1 excitation feature by a Gaussian approximation and the resulting spectrum is presented in Fig. 8(b)

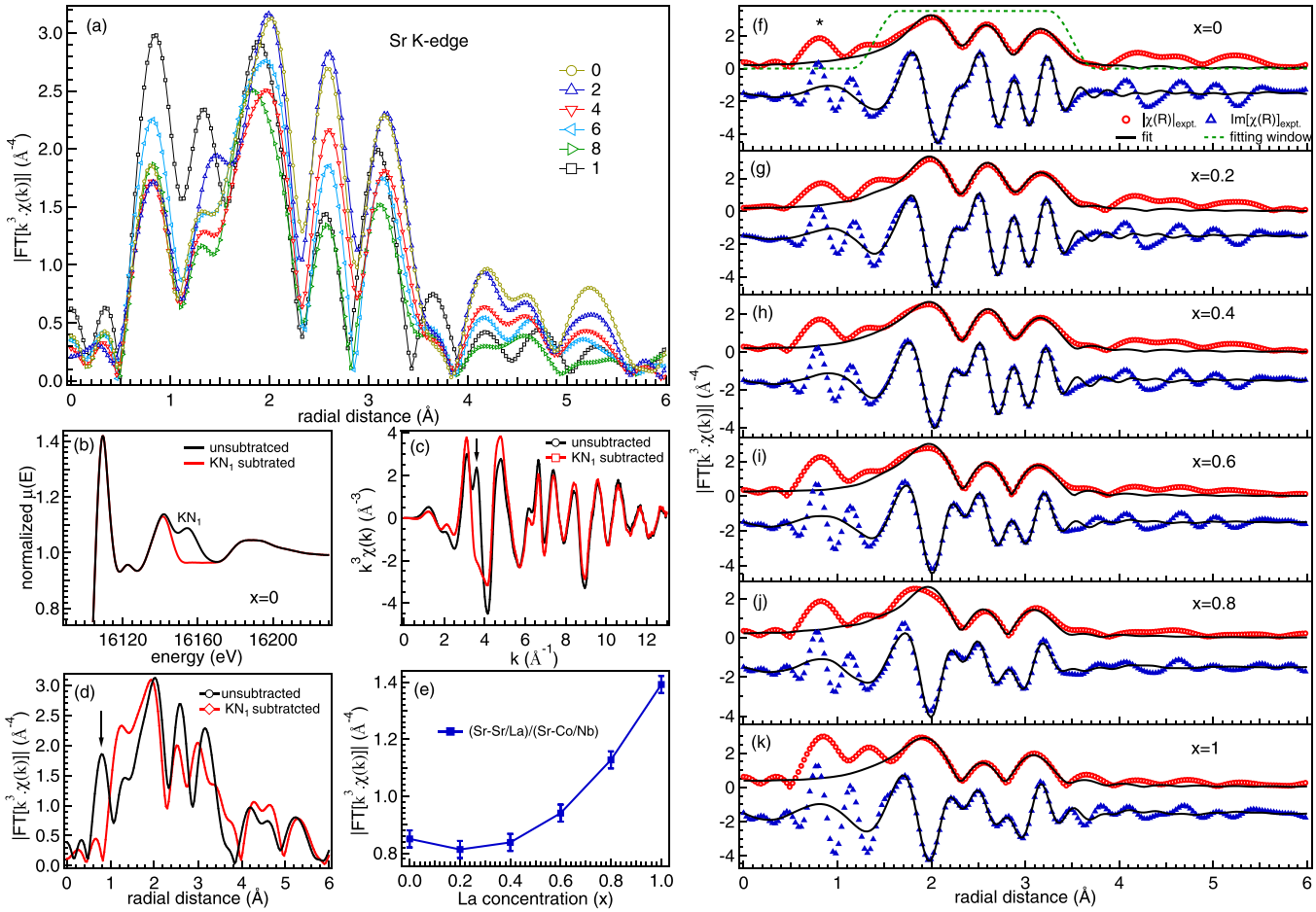

FIG. 8. (a) The magnitude of the Fourier-transformed $k^3\chi(k)$ spectra of Sr K edge for $Sr_{2-x}La_xCoNbO_6$ ($x = 0 - 1$) samples. (b) The enlarged view of the normalized Sr K-edge EXAFS spectra for the $x = 0$ sample, which shows the KN_1 double-electron excitation feature and the resulting spectra after the manual removal of this feature. (c) The k^3 weighted $\chi(k)$ spectra and (d) its Fourier transformation for the $x = 0$ sample before and after the subtraction of the KN_1 excitation feature, where arrows highlight the change in the corresponding features. (e) The ratio of the magnitude of the Sr–Sr/La and Sr–Co/Nb scattering paths as a function of x. (f)–(k) The fitting of the $|\chi(R)|$ and corresponding $\mathrm{Im}[\chi(R)]$ spectra in the window shown by the dotted green line, where the $\mathrm{Im}[\chi(R)]$ spectra in each panel are shifted downward for the clarity in the presentation. The asterisk symbol in (f) represents the peak arising from the KN_1 intra-atomic transition.

for the comparison. We find a clear elimination of a spectral feature around $k = 4$ Å^{-1} as a result of the subtraction of KN_1 double-excitation transition, as highlighted by the arrow in Fig. 8(c) and a well-speculated sharp reduction at around 0.8 Å in the magnitude of Fourier-transformed $k^3\chi(k)$ spectra of Sr K edge in Fig. 8(d). However, the intensity of a few other features also changes as a result of this subtraction, possibly due to inaccuracy in the approximation of KN_1 feature in the spectra resulting from the presence of other nearby spectral features from the local atomic arrangement. Thus, we analyze the as recorded EXAFS spectra of Sr K edge for all the samples by excluding the low radial part of the $|\chi(R)|$ to avoid the contribution from the KN_1 excitation channel. Also, the $KM_{2,3}$ and $KM_{4,5}$ excitations are possible in the Sr K-edge EXAFS spectra resulting from $1s \rightarrow 3p$ and $1s \rightarrow 3d$ transitions, respectively [82]. However, no change is observed in the spectra at their speculated positions from the $Z + 1$ approximation in any of the samples due to dominance of the high-amplitude EXAFS features resulting from the good microcrystalline nature of the samples. However, the effect of these transitions can not be completely neglected in the analysis of the Sr K-edge EXAFS spectra and the data up to very high temperature (>2000 K) are required to fairly quantify their contribution, where structural oscillations significantly diminish due to the enhanced DW factor [85].

Also, we observe three intense features in the Sr K-edge EXAFS spectra between 1.4–3.5 Å for all the samples [see Fig. 8(a)]. These features at around 2, 2.6, and 3.2 Å result from the Sr-O, Sr–Co/Nb, and Sr–Sr/La scattering paths, respectively. Also, a monotonic reduction in the intensity of the peaks corresponding to Sr–Co/Nb and Sr–Sr/La scattering paths is clearly visible with the La substitution [see Fig. 8(a)]. However, a small inconsistency is present in case of the $x = 1$ sample possibly due to the presence of a small amount of oxygen nonstoichiometry, as discussed above. In $I4/m$ symmetry, two different oxygen positions lead to three sets of Sr-O bond distances with four bonds in each group, which further split into 12 different bonds in $P2_1/n$ symmetry [66]. However, we take three Sr-O scattering paths with the same DW factor to fit the Sr K-edge EXAFS spectra in 1.4–3.5 Å range for all the

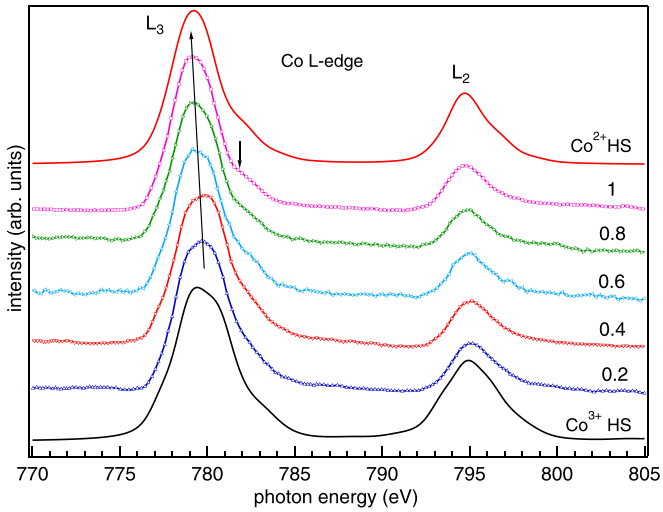

FIG. 9. The Co $L_{2,3}$-edge spectra (vertically offset for clarity) for $Sr_{2-x}La_xCoNbO_6$ samples. The atomic multiplet based simulated spectra for HS Co^{2+} and HS Co^{3+} are compared.

samples, as shown in Figs. 8(f)–8(k) and best-fit parameters are presented in Table I. Further, narrow spatial distribution unable us to distinguish the Sr-Co and Sr-Nb as well as Sr-Sr and Sr-La paths and we take single Sr–Co/Nb and Sr–Sr/La paths for the EXAFS fitting. A reduction in the amplitude of the Sr–Co/Nb and Sr–Sr/La peaks indicates the distortions in the corresponding scattering paths with the La substitution, which is reflected into their corresponding Debye-Waller factors, as presented in Table I. This effect is more prominent in case of Sr–Co/Nb as compared to Sr–Sr/La scattering path, which is clear in the plot of amplitude ratio of these two scattering paths [(Sr–Sr/La)/(Sr–Co/Nb)] particularly for the $x \geqslant 0.6$ samples [see Fig. 8(e)]. The change in formal charge and ionic radii of *A*- and *B*-site atoms causes the reduction in amplitude of their respective scattering paths with x. Further, the different tendency of the Nb–Sr/La (increasing) and Co–Sr/La (decreasing) SS paths with x is evident from the Nb and Co *K*-edge EXAFS spectra, respectively, results in the spatially wide distribution and hence more rapid reduction in the intensity of Sr–Co/Nb path as compared to Sr–Sr/La with x. This behavior suggests that the chemical pressure due to La substitution induces more distortion at the *A* site as compared to the *B* site(s), and results in the evolution of complex magnetic interactions [9,25].

Finally, we present the Co $L_{2,3}$ soft-XAS spectra in Fig. 9 where transition from two spin-orbit splitting components of Co $2p$ final states, i.e., $2p_{3/2} \rightarrow 3d$ (L_3) and $2p_{1/2} \rightarrow 3d$ (L_2), are observed around 780 and 795 eV, respectively, for all the samples. These peaks shift to the lower energy (as indicated by the arrow for the L_3 edge), which indicates the enhancement in the concentration of Co^{2+} with the La substitution. A shift of 0.6(1) eV from the $x = 0.2$ to 1 sample in the L_3 white line gives +2.3(1) valence state of Co in the $x = 1$ sample [33] by considering the $Co^{2.8+}$ for the $x = 0.2$ sample. This is also consistent with the Co *K*-edge XANES spectra, discussed above. Interestingly, we observe the consistent reduction in the broadening with the evolution of a hump at the shoulder of L_3 edge with the La substitution, as indicated by the vertical arrow for the $x = 1$ sample. To understand the physical origin of this, we simulate the *L*-edge XAS spectra for HS Co^{2+} and HS Co^{3+} using the CTM4XAS software. A charge-transfer effect from oxygen to Co atoms was also introduced in the simulation for both valence states of Co, resulting in the additional $2p^63d^7\underline{L}^1 \rightarrow 2p^53d^8\underline{L}^1$ and $2p^63d^8\underline{L}^1 \rightarrow 2p^53d^9\underline{L}^1$ transitions in case of Co^{3+} and Co^{2+}, respectively. The Lorentzian and Gaussian line shapes with half-width of 0.5 and 0.45 eV were used to account for the core-hole lifetime and instrumental broadening. The crystal field-field splitting ($10Dq$), onsite Coulomb correlation energy of $3d$ electrons (U_{dd}), core-hole potential (U_{pd}), charge-transfer energy (Δ_{ct}), and O $2p$–Co $3d$ hybridization strength parameters were varied to best match the experimental and simulated spectra. The intra-atomic interactions were approximated by reducing the Slater integrals to 80% from their Hartree-Fock values. The best matched parameters are $10Dq = 1.3$ and 0.5 eV, $U_{dd} - U_{pd} = 3.0$ and 0.2 eV, and $\Delta_{ct} = -6.5$ and 1.4 eV for HS Co^{3+} and HS Co^{2+} spectra, respectively. The *p-d* hybridization strength parameters $T_{e_g} = 2.0$ and 0.8 and $T_{t_{2g}} = 1.0$ and 0.4 were used for Co^{3+} and Co^{2+}, respectively and the resulting spectra are presented in Fig. 9. The extracted value of $10Dq$ for Co^{3+} is smaller than that of $LaCoO_3$ (~2.3 eV [13]), indicating the higher probability of finding Co^{3+} in the IS/HS state, which is consistent with the magnetization results [9,86]. Further, the large negative value of the charge-transfer energy indicates the highly covalent nature of the Co-O bonds, where the covalency character decreases with the La substitution. Moreover, the branching ratios, defined as $(BR) = I(L_3)/[I(L_2) + I(L_3)]$, where $I(L_2)$ and $I(L_3)$ represent the integrated intensity of L_2 and L_3 edges, is 0.757, 0.786, 0.764, 0.763, and 0.758 for the $x = 0.2$–1 samples, respectively. These preliminary results of SXAS further suggest for the mixed IS and HS states of Co^{3+} in $Sr_{2-x}La_xCoNbO_6$ samples [87]. However, high-resolution SXAS measurements can be further useful to understand the complex spin-state transition in these samples as a function of x and temperature [6,9,33].

IV. CONCLUSIONS

We have investigated the electronic and local structure of $Sr_{2-x}La_xCoNbO_6$ ($x = 0$–1) samples using detailed analysis of XANES and EXAFS spectra as well as the simulation of Nb, Co, and Sr *K* edges. A very weak pre-edge feature in case of Nb *K*-edge XANES spectra indicates the negligible off-center displacement of Nb atoms in the NbO_6 octahedra. This pre-edge feature results from the transition of $1s$ electrons to the $4d$ states of Nb mixed with Nb and/or O p states. Also, the intensity of pre-edge features of Co *K*-edge spectra depends on the number of $3d$ electrons, but analysis discards their pure quadruple origin. Moreover, the significantly strong pre-edge feature in case of Co *K*-edge XANES spectra as compared to Nb indicates the presence of Co and Nb atoms in the different octahedral environment. The Co *K*-edge XANES spectra indicate a change in valence state of Co from 3+ towards 2+ with the La substitution (x). However, an oxidation of Co is observed in the $x = 0.8$ and 1 samples, which can be attributed to the presence of a small amount of oxygen nonstoichiometry in these La-rich samples. The divalent state

of Sr and pentavalent state of Nb are found to remain invariant with the La substitution. The EXAFS measurements evidence a decrease in the local distortion around *B*-site atoms, despite reduction in the overall crystal symmetry with the La substitution. The *z*-out JT distortion in CoO_6 and consequently *z*-in distortion in the NbO_6 octahedra have been observed in all the samples. The distortion in the CoO_6 octahedra decreases monotonically with the La substitution due to increase in the concentration of JT inactive Co^{2+} ions, whereas that in NbO_6 octahedra remains almost invariant up to $x = 0.4$, and then decreases for higher La concentration. This abrupt change in the local coordination environment around the Nb atoms results in the sharp enhancement in *B*-site ordering and hence evolution of AFM interactions in the $x \geqslant 0.6$ samples. This is further supported by sudden enhancement in the longer Nb–Co2/Nb2 path for the $x \geqslant 0.6$ samples in the higher coordination shell in Nb *K*-edge EXAFS spectra. Interestingly, we observe a strong correlation between the degree of octahedral distortion in $(Co/Nb)O_6$ units and intensity of their respective white-line features. An increase in the degree of octahedral distortion is found to enhance the metal-ligand overlapping and delocalization of the TM *p* states, resulting in the low intense broad white-line features in their *K*-edge XANES spectra. We reveal that such a correlation is useful to estimate the extent of octahedral distortion in the complex compounds directly from the analysis of XANES spectra. Moreover, the Sr *K*-edge absorption spectra show clear evidence of the KN_1 double-electron excitation for all the samples, suggesting the necessity of the careful treatment of the Sr *K*-edge EXAFS spectra. Finally, the Co $L_{2,3}$-edge spectra indicate the decrease in the crystal-field strength and tendency of O to Co charge transfer with *x*.

ACKNOWLEDGMENTS

A.K. and R.S. thank the UGC and DST-Inspire for the fellowship. We thank J. J. Rehr for very useful discussions on the XANES simulations using FEFF code. Authors also acknowledge D. M. Phase and R. K. Sah for support and help, respectively, during the soft XAS measurements. We acknowledge the financial support from SERB-DST through core research grant (Project Reference No. CRG/2020/003436). We also greatly acknowledge the CRS (Project No. CSR-ICISUM-36/CRS-319/2019-20/1371) for collaborative research work.

[1] F. E. Mabbs and D. J. Machin, *Magnetism and Transition Metal Complexes* (Chapman and Hall, London, 1973).

[2] F. Lloret, M. Julve, J. Cano, R. Ruiz-García, and E. Pardo, Magnetic properties of six-coordinated high-spin Co(II) complexes: theoretical background and its application, Inorganica Chim. Acta **361**, 3432 (2008).

[3] H. Liu and G. Khaliullin, Pseudospin exchange interactions in d^7 cobalt compounds: Possible realization of the Kitaev model, Phys. Rev. B **97**, 014407 (2018).

[4] P. M. Raccah and J. B. Goodenough, First-order localized-electron ⇆ collective-electron transition in $LaCoO_3$, Phys. Rev. **155**, 932 (1967).

[5] G. Vankó, J.-P. Rueff, A. Mattila, Z. Németh, and A. Shukla, Temperature- and pressure-induced spin-state transitions in $LaCoO_3$, Phys. Rev. B **73**, 024424 (2006).

[6] M. Merz, D. Fuchs, A. Assmann, S. Uebe, H. v. Löhneysen, P. Nagel, and S. Schuppler, Spin and orbital states in single-layered $La_{2-x}Ca_xCoO_4$ studied by doping- and temperature-dependent near-edge x-ray absorption fine structure, Phys. Rev. B **84**, 014436 (2011).

[7] J.-M. Chen, Y.-Y. Chin, M. Valldor, Z. Hu, J.-M. Lee, S.-C. Haw, N. Hiraoka, H. Ishii, C.-W. Pao, K.-D. Tsuei, J.-F. Lee, H.-J. Lin, L.-Y. Jang, A. Tanaka, C.-T. Chen, and L. H. Tjeng, A complete high-to-low spin state transition of trivalent cobalt ion in octahedral symmetry in $SrCo_{0.5}Ru_{0.5}O_{3-\delta}$, J. Am. Chem. Soc. **136**, 1514 (2014).

[8] K. Knížek, P. Novák, and Z. Jirák, Spin state of $LaCoO_3$: Dependence on CoO_6 octahedra geometry, Phys. Rev. B **71**, 054420 (2005).

[9] A. Kumar and R. S. Dhaka, Unraveling magnetic interactions and the spin state in insulating $Sr_{2-x}La_xCoNbO_6$, Phys. Rev. B **101**, 094434 (2020).

[10] S. Tao and J. T. S. Irvine, A redox-stable efficient anode for solid-oxide fuel cells, Nat. Mater. **2**, 320 (2003).

[11] J. Chakrabartty, C. Harnagea, M. Celikin, F. Rosei, and R. Nechache, Improved photovoltaic performance from inorganic perovskite oxide thin films with mixed crystal phases, Nat. Photon. **12**, 271 (2018).

[12] V. Krayzman, I. Levin, J. C. Woicik, D. Yoder, and D. A. Fischer, Effects of local atomic order on the pre-edge structure in the Ti *K* x-ray absorption spectra of perovskite $CaTi_{1-x}Zr_xO_3$, Phys. Rev. B **74**, 224104 (2006).

[13] M. Medarde, C. Dallera, M. Grioni, J. Voigt, A. Podlesnyak, E. Pomjakushina, K. Conder, Th. Neisius, O. Tjernberg, and S. N. Barilo, Low-temperature spin-state transition in $LaCoO_3$ investigated using resonant x-ray absorption at the Co K edge, Phys. Rev. B **73**, 054424 (2006).

[14] R. Shukla and R. S. Dhaka, Anomalous magnetic and spin glass behavior in Nb substituted $LaCo_{1-x}Nb_xO_3$, Phys. Rev. B **97**, 024430 (2018).

[15] S. Vasala and M. Karppinen, $A_2B'B''O_6$ perovskites: A review, Prog. Solid State Chem. **43**, 1 (2015).

[16] D. Niebieskikwiat, F. Prado, A. Caneiro, and R. D. Sánchez, Antisite defects versus grain boundary competition in the tunneling magnetoresistance of Sr_2FeMoO_6 double perovskite, Phys. Rev. B **70**, 132412 (2004).

[17] D. Sánchez, J. A. Alonso, M. García-Hernández, M. J. Martínez-Lope, J. L. Martínez, and A. Mellergård, Origin of neutron magnetic scattering in antisite-disordered Sr_2FeMoO_6 double perovskites, Phys. Rev. B **65**, 104426 (2002).

[18] A. Jung, I. Bonn, V. Ksenofontov, M. Panthöfer, S. Reiman, C. Felser, and W. Tremel, Effect of cation disorder on the magnetic properties of $Sr_2Fe_{1-x}GaxReO_6$ ($0 < x < 0.7$) double perovskites, Phys. Rev. B **75**, 184409 (2007).

[19] O. Erten, O. N. Meetei, A. Mukherjee, M. Randeria, N. Trivedi, and P. Woodward, Theory of Half-Metallic Ferrimagnetism in Double Perovskites, Phys. Rev. Lett. **107**, 257201 (2011).

[20] C. Frontera and J. Fontcuberta, Configurational disorder and magnetism in double perovskites: A Monte Carlo simulation study, Phys. Rev. B **69**, 014406 (2004).

[21] M. Das, P. Dutta, S. Giri, S. Majumdar, A. Bandyopadhyay, A. K. Yadav, S. N. Jha, D. Bhattacharyya, G. Das, and V. Rajaji, Cationic disorder: A pathway for demonstrating inverse exchange bias in Gd_2CoRuO_6, Phys. Rev. B **101**, 064419 (2020).

[22] M. T. Azcondo, J. R. de Paz, K. Boulahya, C. Ritter, F. García-Alvarado, and U. Amador, Complex magnetic behaviour of $Sr_2CoNb_{1-x}Ti_xO_6$ ($0 \leqslant x \leqslant 0.5$) as a result of a flexible microstructure, Dalton Trans. **44**, 3801 (2015).

[23] G. J. Wang, C. C. Wang, S. G. Huang, X. H. Sun, C. M. Lei, T. Li, and L. N. Liu, Origin of the colossal dielectric properties in double-perovskite Sr_2CoNbO_6, AIP Adv. **3**, 022109 (2013).

[24] J. Bashir and R. Shaheen, Structural and complex AC impedance spectroscopic studies of A_2CoNbO_6 (A = Sr, Ba) ordered double perovskites, Solid State Sci. **13**, 993 (2011).

[25] A. Kumar, B. Schwarz, H. Ehrenberg, and R. S. Dhaka, Evidence of discrete energy states and cluster-glass behavior in $Sr_{2-x}La_xCoNbO_6$, Phys. Rev. B **102**, 184414 (2020).

[26] J.-W. G. Bos and J. P. Attfield, Magnetic frustration in La(A)$CoNbO_6$ (A=Ca, Sr, and Ba) double perovskites, Phys. Rev. B **70**, 174434 (2004).

[27] G. Bunker, *Introduction to XAFS: A Practical Guide to X-ray Absorption Fine Structure Spectroscopy* (Cambridge University Press, Cambridge, 2010).

[28] K. Klementiev and R. Chernikov, XAFSmass: a program for calculating the optimal mass of XAFS samples, J. Phys.: Conf. Ser. **712**, 012008 (2016).

[29] S. Basu, C. Nayak, A. K. Yadav, A. Agrawal, A. K. Poswal, D. Bhattacharyya, S. N. Jha, and N. K. Sahoo, A comprehensive facility for EXAFS measurements at the INDUS-2 synchrotron source at RRCAT, Indore, India, J. Phys.: Conf. Ser. **493**, 012032 (2014).

[30] N. Sahai, S. A. Carroll, S. Roberts, and P. A. O'Day, X-ray absorption spectroscopy of strontium (II) coordination, J. Colloid Interface Sci. **222**, 198 (2000).

[31] J. J. Rehr, J. J. Kas, F. D. Vila, M. P. Prange, and K. Jorissen, Parameter-free calculations of x-ray spectra with FEFF9, Phys. Chem. Chem. Phys. **12**, 5503 (2010).

[32] J. J. Rehr and R. C. Albers, Theoretical approaches to x-ray absorption fine structure, Rev. Mod. Phys. **72**, 621 (2000).

[33] T. Burnus, Z. Hu, H. H. Hsieh, V. L. J. Joly, P. A. Joy, M. W. Haverkort, H. Wu, A. Tanaka, H.-J. Lin, C. T. Chen, and L. H. Tjeng, Local electronic structure and magnetic properties of $LaMn_{0.5}Co_{0.5}O_3$ studied by x-ray absorption and magnetic circular dichroism spectroscopy, Phys. Rev. B **77**, 125124 (2008).

[34] F. M. F. de Groot, J. C. Fuggle, B. T. Thole, and G. A. Sawatzky, $2p$ x-ray absorption of $3d$ transition-metal compounds: An atomic multiplet description including the crystal field, Phys. Rev. B **42**, 5459 (1990).

[35] E. Stavitski and F. M. F. de Groot, The CTM4XAS program for EELS and XAS spectral shape analysis of transition metal L edges, Micron **41**, 687 (2010).

[36] T. Yamamoto, Assignment of pre-edge peaks in K-edge x-ray absorption spectra of 3d transition metal compounds: electric dipole or quadrupole?, X-Ray Spectrom. **37**, 572 (2008).

[37] F. Farges, G. E. Brown, Jr., and J. J. Rehr, Ti K-edge XANES studies of Ti coordination and disorder in oxide compounds: Comparison between theory and experiment, Phys. Rev. B **56**, 1809 (1997).

[38] Y. Joly, D. Cabaret, H. Renevier, and C. R. Natoli, Electron Population Analysis by Full-Potential X-Ray Absorption Simulations, Phys. Rev. Lett. **82**, 2398 (1999).

[39] A. I. Frenkel, D. M. Pease, J. Giniewicz, E. A. Stern, D. L. Brewe, M. Daniel, and J. Budnick, Concentration-dependent short-range order in the relaxor ferroelectric (1-x)Pb(Sc, Ta)O_3-xPbTiO_3, Phys. Rev. B **70**, 014106 (2004).

[40] R. V. Vedrinskii, V. L. Kraizman, A. A. Novakovich, Ph. V. Demekhin, and S. V. Urazhdin, Pre-edge fine structure of the $3d$ atom K x-ray absorption spectra and quantitative atomic structure determinations for ferroelectric perovskite structure crystals, J. Phys.: Condens. Matter **10**, 9561 (1998).

[41] B. Ravel, E. A. Stern, R. I. Vedrinskii, and V. Kraizman, Local structure and the phase transitions of $BaTiO_3$, Ferroelectrics **206**, 407 (1998).

[42] See Supplemental Material at http://link.aps.org/supplemental/10.1103/PhysRevB.105.245155 for supporting data, details of analysis, and fitting parameters of XAS spectra, which also includes Refs. [43–45].

[43] B. Ravel and M. Newville, ATHENA, ARTEMIS, HEPHAESTUS: Data analysis for X-ray absorption spectroscopy using IFEFFIT, J. Synchrotron Radiat. **12**, 537 (2005).

[44] F. Frati, M. O. J. Y. Hunault, and F. M. F. de Groot, Oxygen K–edge X–ray Absorption Spectra, Chem. Rev. **120**, 4056 (2020).

[45] J. Suntivich, W. T. Hong, Y.-L. Lee, J. M. Rondinelli, W. Yang, J. B. Goodenough, B. Dabrowski, J. W. Freeland, and Y. Shao-Horn, Estimating Hybridization of Transition Metal and Oxygen States in Perovskites from O K-edge X-ray Absorption Spectroscopy, J. Phys. Chem. C **118**, 1856 (2014).

[46] M. W. Ruckman, G. Reisfeld, N. M. Jisrawi, M. Weinert, M. Strongin, H. Wiesmann, M. Croft, A. Sahiner, D. Sills, and P. Ansari, XANES study of hydrogen incorporation in a Pd-capped Nb thin film, Phys. Rev. B **57**, 3881 (1998).

[47] F. W. Lytle, R. B. Greegor, and A. J. Panson, Discussion of x-ray-absorption near-edge structure: Application to Cu in the high-T_c, superconductors $La_{1.8}Sr_{0.2}CuO_4$ and $YBa_2Cu_3O_7$, Phys. Rev. B **37**, 1550 (1988).

[48] C. Marini, O. Noked, I. Kantor, B. Joseph, O. Mathon, R. Shuker, B. J. Kennedy, S. Pascarelli, and E. Sterer, Nb K-edge x-ray absorption investigation of the pressure induced amorphization in A-site deficient double perovskite $La_{1/3}NbO_3$, J. Phys.: Condens. Matter **28**, 045401 (2016).

[49] M.-C. Lee, S. Lee, C. J. Won, K. D. Lee, N. Hur, J.-L Chen, D.-Y Cho, and T. W. Noh, Hybridized orbital states in spin-orbit coupled 3d–5d double perovskites studied by x-ray absorption spectroscopy, Phys. Rev. B **97**, 125123 (2018).

[50] Z. Y. Wu, D. C. Xian, T. D. Hu, Y. N. Xie, Y. Tao, C. R. Natoli, E. Paris, and A. Marcelli, Quadrupolar transitions and medium-range-order effects in metal K-edge x-ray absorption spectra of 3d transition-metal compounds, Phys. Rev. B **70**, 033104 (2004).

[51] N. Ishimatsu, T. Watanabe, K. Oka, M. Azuma, M. Mizumaki, K. Nitta, T. Ina, and N. Kawamura, Differences in local structure around Co and Fe of the $BiCo_{1-x}Fe_xO_3$ system determined by x-ray absorption fine structure, Phys. Rev. B **92**, 054108 (2015).

[52] M. E. Lines and A. M. Glass, *Principles and Applications of Ferroelectrics and Related Materials* (Clarendon Press, Oxford, 1977).

[53] O. Haas, R. P. W. J. Struis, and J. M. McBreen, Synchrotron X-ray absorption of $LaCoO_3$ perovskite, J. Solid State Chem. **177**, 1000 (2004).

[54] G. Vankó, F. M. F. de Groot, S. Huotari, R. J. Cava, T. Lorenz, and M. Reuther, Intersite 4*p*-3*d* hybridization in cobalt oxides: a resonant x-ray emission spectroscopy study, arXiv:0802.2744.

[55] G. E. Sterbinsky, P. J. Ryan, J.-W. Kim, E. Karapetrova, J. X. Ma, J. Shi, and J. C. Woicik, Local atomic and electronic structures of epitaxial strained $LaCoO_3$ thin films, Phys. Rev. B **85**, 020403(R) (2012).

[56] A. Chainani, M. Mathew, and D. D. Sarma, Electron-spectroscopy study of the semiconductor-metal transition in $La_{1-x}Sr_xCo_3$, Phys. Rev. B **46**, 9976 (1992).

[57] J. Blasco, J. M. Michalik, J. García, G. Subías, and J. M. De Teresa, Effects of the lanthanide addition to the Sr_2CrReO_6 double perovskite, Phys. Rev. B **76**, 144402 (2007).

[58] R. Shukla, A. Kumar, R. Kumar, S. N. Jha, and R. S. Dhaka, X-ray absorption spectroscopy study of $La_{1-y}Sr_yCo_{1-x}Nb_xO_3$, J. Phys. Chem. C **125**, 10130 (2021).

[59] G. Subías, J. Blasco, S. Lafuerza, V. Cuartero, M. C. Sánchez, R. Boada, S. Díaz-Moreno, F. Fauth, and J. García, Relation among oxygen stoichiometry, structure, and Co valence and spin state in single-layer $La_{2-x}A_xCoO_{4\pm\delta}$ (A= Ca, Sr) perovskites, Inorg. Chem. **59**, 15757 (2020).

[60] V. Cuartero, S. Lafuerza, M. Rovezzi, J. García, J. Blasco, G. Subías, and E. Jimenez, X-ray absorption and emission spectroscopy study of Mn and Co valence and spin states in $TbMn_{1-x}Co_xO_3$, Phys. Rev. B **94**, 155117 (2016).

[61] J. García, G. Subías, V. Cuartero, and J. Herrero-Martin, On the correlation between the X-ray absorption chemical shift and the formal valence state in mixed-valence manganites, J. Synchrotron Rad. **17**, 386 (2010).

[62] G. Subías, J. García, J. Blasco, and M. G. Proietti, Effect of cation vacancies in the local structure and transport properties of $LaMnO_{3+\delta}$: A Mn K-edge x-ray-absorption study, Phys. Rev. B **58**, 9287 (1998).

[63] R. I. Dass, J.-Q. Yan, and J. B. Goodenough, Oxygen stoichiometry, ferromagnetism, and transport properties of $La_{2-x}NiMnO_{6+\delta}$, Phys. Rev. B **68**, 064415 (2003).

[64] M. C. Sánchez, J. García, J. Blasco, G. Subías, and J. Perez-Cacho, Local electronic and geometrical structure of $LaNi_{1-x}Mn_xO_{3+\delta}$ perovskites determined by x-ray-absorption spectroscopy, Phys. Rev. B **65**, 144409 (2002).

[65] M. B. Robin and P. Day, Mixed valence chemistry: A survey and classification, Adv. Inorg. Chem. Radiochem. **10**, 247 (1968).

[66] Ajay Kumar, A. Jain, S. M. Yusuf, and R. S. Dhaka, Observation of anisotropic thermal expansion and Jahn-Teller effect in double perovskites $Sr_{2-x}La_xCoNbO_6$ using neutron diffraction, J. Phys. Chem. Lett. **13**, 3023 (2022).

[67] M. Altarelli, D. L. Dexter, H. M. Nussenzveig, and D. Y. Smith, Superconvergence and sum rules for the optical constants, Phys. Rev. B **6**, 4502 (1972).

[68] S. K. Pandey, S. Khalid, N. P. Lalla, and A. V. Pimpale, Local distortion in $LaCoO_3$ and $PrCoO_3$: extended x-ray absorption fine structure, x-ray diffraction and x-ray absorption near edge structure studies, J. Phys.: Condens. Matter **18**, 10617 (2006).

[69] Z. Tan, M. E. Filipkowski, J. I. Budnick, E. K. Heller, D. L. Brewe, B. L. Chamberland, C. E. Bouldin, J. C. Woicik, and D. Shi, Strontium-Induced Oxygen Defect Structure and Hole Doping in $La_{2-x}Sr_xCuO_4$, Phys. Rev. Lett. **64**, 2715 (1990).

[70] Z. Y. Wu, M. Benfatto, and C. R. Natoli, Theoretical analysis of x-ray-absorption near-edge structure at the Sr *K* edge in $La_{2-x}Sr_xCuO_4$ compounds, Phys. Rev. B **45**, 531(R) (1992).

[71] E. A. Hudson, P. G. Allen, L. J. Terminello, M. A. Denecke, and T. Reich, Polarized x-ray-absorption spectroscopy of the uranyl ion: Comparison of experiment and theory, Phys. Rev. B **54**, 156 (1996).

[72] Y. Zhu, S. Wu, B. Tu, S. Jin, A. Huq, J. Persson, H. Gao, D. Ouyang, Z. He, D.-X. Yao, Z. Tang, and H.-F. Li, High-temperature magnetism and crystallography of a $YCrO_3$ single crystal, Phys. Rev. B **101**, 014114 (2020).

[73] R. D. Shannon, Revised effective ionic radii and systematic studies of interatomic distances in halides and chalcogenides, Acta. Crystallogr. A **32**, 751 (1976).

[74] M. A. Laguna-Marco, E. Arias-Egido, C. Piquer, V. Cuartero, L. Hernández-López, P. Kayser, J. A. Alonso, J. A. T. Barker, G. Fabbris, C. A. Escanhoela Jr., and T. Irifune, Magnetism of Ir^{5+}-based double perovskites: Unraveling its nature and the influence of structure, Phys. Rev. B **101**, 014449 (2020).

[75] A. Bandyopadhyay, S. Kumar Neogi, A. Paul, C. Meneghini, I. Dasgupta, S. Bandyopadhyay, and S. Ray, Cationic order versus La-O covalency in LaA(Ca, Ba)$VMoO_6$ double perovskites, Phys. Rev. B **95**, 024432 (2017).

[76] S. Yamaguchi, Y. Okimoto, and Y. Tokura, Local lattice distortion during the spin-state transition in $LaCoO_3$, Phys. Rev. B **55**, R8666 (1997).

[77] S. K. Pandey, A. Kumar, S. Patil, V. R. R. Medicherla, R. S. Singh, K. Maiti, D. Prabhakaran, A. T. Boothroyd, and A. V. Pimpale, Investigation of the spin state of Co in $LaCoO_3$ at room temperature: *Ab initio* calculations and high-resolution photoemission spectroscopy of single crystals, Phys. Rev. B **77**, 045123 (2008).

[78] H. Hsu, K. Umemoto, M. Cococcioni, and R. Wentzcovitch, First-principles study for low-spin $LaCoO_3$ with a structurally consistent Hubbard U, Phys. Rev. B **79**, 125124 (2009).

[79] A. I. Nesvizhskii, A. L. Ankudinov, and J. J. Rehr, Normalization and convergence of x-ray absorption sum rules, Phys. Rev. B **63**, 094412 (2001).

[80] H. Modrow, S. Bucher, J. J. Rehr, and A. L. Ankudinov, Calculation and interpretation of K-shell x-ray absorption near-edge structure of transition metal oxides, Phys. Rev. B **67**, 035123 (2003).

[81] A. L. Ankudinov, B. Ravel, J. J. Rehr, and S. D. Conradson, Real-space multiple-scattering calculation and interpretation of x-ray-absorption near-edge structure, Phys. Rev. B **58**, 7565 (1998).

[82] P. D'Angelo, H.-F. Nolting, and N. V. Pavel, Evidence for multielectron resonances at the Sr K edge, Phys. Rev. A **53**, 798 (1996).

[83] P. D'Angelo, A. Di Cicco, A. Filipponi, and N. V. Pavel, Double-electron excitation channels at the Br K edge of HBr and Br_2, Phys. Rev. A **47**, 2055 (1993).

[84] G. Li, F. Bridges, and G. S. Brown, Multielectron X-Ray Photoexcitation Observations in X-Ray-Absorption Fine-Structure Background, Phys. Rev. Lett. **68**, 1609 (1992).

[85] A. Filipponi and A. Di Cicco, Atomic background in w-ray absorption spectra of fifth-period elements: Evidence for double-electron excitation edges, Phys. Rev. A **52**, 1072 (1995).

[86] K. Yoshii, Structural and magnetic properties of the perovskites $Sr_{n+1}(Co_{0.5}Nb_{0.5})_nO_{3n+1}$ ($n = \infty$, 2, and 1), J. Alloys Compd. **307**, 119 (2000).

[87] B. T. Thole and G. V. D. Laan, Branching ratio in X-ray absorption spectroscopy, Phys. Rev. B **38**, 3158 (1988).